IDŐJÁRÁS

QUARTERLY JOURNAL
OF THE HUNGARIAN METEOROLOGICAL SERVICE

CONTENTS

****

http://www.met.hu/firat/ido-e.html

VOL. 104 * NO. 2 * APRIL–JUNE 2000

IDŐJÁRÁS

Quarterly Journal of the Hungarian Meteorological Service

Editorial Office: P.O. Box 39, H-1675 Budapest, Hungary or
Gilice tér 39, H-1181 Budapest, Hungary
E-mail: prager@met.hu or *antal@met.hu*
Fax: (36-1) 290-7387

Subscription by

mail: IDŐJÁRÁS, P.O. Box 39, H-1675 Budapest, Hungary;
E-mail: prager@met.hu or *antal@met.hu*; *Fax: (36-1) 290-7387*

IDŐJÁRÁS

Quarterly Journal of the Hungarian Meteorological Service
Vol. 104, No. 2, April–June 2000, pp. 67–89

New methods for severe precipitation warning for Hungary

Ágnes Takács[1], Cecilia Girz[2], Edward Tollerud[2] and Sándor Kertész[1]

[1]*Hungarian Meteorological Service, H-1525 Budapest, P.O. Box 38, Hungary;*
E-mail: takacs@fsl.noaa.gov, kertesz.s@met.hu
[2]*NOAA/OAR Forecast Systems Laboratory, 325 Broadway, Mail Code: R/FS1,*
80303 Boulder, Colorado, United States of America
E-mail: girz@fsl.noaa.gov, tollerud@fsl.noaa.gov

(Manuscript submitted for publication 5 November 1999; in final form 17 April 2000)

Abstract—Under a project funded by the United States–Hungarian Science and Technology Joint Fund, research has been conducted to improve the forecasting of extreme rainfall events (often accompanied by flash flooding) in Hungary. Many of these events appear to result from mesoscale circulations, possibly small mesoscale convective systems (MCSs), thus presenting a very challenging forecast problem. Two keys to improving these forecasts are (1) a better physical understanding of the mesoscale circulations that produce severe rainfall, and (2) improved methods to identify and monitor the evolution of potentially dangerous systems as early in their development as possible. Three areas of research have been pursued. First, a variant of the Probable Maximum Precipitation (PMP), the *Possible* Maximum Precipitation (PoMP), has been derived and then employed retrospectively in the diagnosis of several incidents of extreme precipitation that occurred in Hungary during the summer of 1998. One of the events studied, a case of very heavy rainfall in Mosonmagyaróvár on 27 July, is described in detail. In this event as well as the others, PoMP results showed promise as a way to estimate potential severe rainfall. A second area of research involved the implementation and testing of an automated satellite rain estimation technique. Observations from the European Meteorological Satellite (METEOSAT) were used daily to provide precipitation fields over Hungary and neighboring countries. Detailed analyses were made of the extreme precipitation events. Precipitation patterns were generally very widespread and satellite estimates compared poorly with gauge data. Possible reasons for these discrepancies included errors arising from the quality and frequency of the satellite data, questionable applicability of rain-estimation parameters in the mountainous regions surrounding the Carpathian Basin, and the frequent occurrence of embedded convection in these cases. A third area of research involved attempts to qualitatively assess the frequency of occurrence of large MCSs. Although some statistical evidence (primarily the existence of nocturnal maxima of heavy precipitation rates in some regions of Hungary) suggested the existence of MCSs, a qualitative examination of satellite and radar observations during two summers (1997 and 1998) did not uncover the characteristic signatures of Mesoscale Convective Complexes (MCCs), the largest MCSs.

Key-words: flood warning, hydrometeorological techniques, satellite rain estimates, possible maximum precipitation, heavy precipitation, diurnal variation of precipitation.

1. Introduction

Severe weather causes substantial loss of life and much material damage in Hungary. One of the most damaging severe-weather-caused events is extreme rainfall which can produce flash floods, or overflow storm sewers in urban areas. These types of heavy precipitation events are often mesoscale in nature, and therefore present an important challenge to forecasters. Two keys to improving these difficult forecasts are (1) better physical understanding, and (2) improved methods to identify and monitor the evolution and precipitation of potentially dangerous systems as early as possible. This paper describes research intended to advance both these areas.

In Section 2 we present statistical results that address (1) by describing diurnal and other aspects of heavy precipitation events in Hungary. In particular, we discuss the possible contribution of mesoscale convective complexes (MCCs) to dangerous precipitation in Hungary. To address (2), we have developed a forecasting method involving two components: Possible Maximum Precipitation (PoMP) computations and satellite rainfall estimates. Section 3 includes a discussion of the PoMP and the PMP, from which it was derived, and the operational measurements it requires. An earlier application of the method is presented in *Takács et al.* (1998). In Section 4 we describe how we adapted the Griffith-Woodley satellite rainfall estimation technique to make it applicable to conditions in Hungary. Use of pseudo-soundings from runs of the Aladin NWP model (*Horányi et al.*, 1996) is a novel feature of this application. A case study of a heavy precipitation event on 27 and 28 July 1998 in northeast Hungary illustrating this procedure is presented in Section 5.

This paper documents results of a three-year project sponsored by the United States-Hungarian Science and Technology Joint Fund. The reader will find that despite the demonstration of promise of new forecasting techniques, several substantive questions could not be answered by the end of the three years. For these aspects of unfinished research, we have indicated the path that we think is the most fruitful for resolving the issues.

2. Characteristics of heavy precipitation events in Hungary

During background research for this study, we performed statistical analyses of precipitation events in Hungary[1]. To study precipitation intensity and duration,

[1] Results of this research are described in the unpublished manuscript *Development of a warning system for quantitative prediction of heavy rainfall*, the Final Report for the research project entitled "Improvement of meteorological forecasts for hydrological purposes", sponsored by the Ministry of Environment Protection and Water Management, Budapest, 1989, Á. Takács, Project Leader.

we examined several years of short-term precipitation data extracted from paper charts at Hungarian recording stations, concentrating on locally heavy precipitation during a five-year period between 1985 and 1989. Because it was fundamentally important to consider the temporal distribution of precipitation, we only included events during which the core of the precipitation system could be shown to be located over recording stations. This reduced the total possible number of events that we could investigate to 93.

We derived the following information from the precipitation chart recordings:

- start time of heavy precipitation,
- system duration (in tenths of hours),
- total amount of precipitation produced by the system (in mm),
- average intensity of the entire system (in mm h^{-1}),
- duration of the most intense period within the system (in minutes),
- amount of precipitation during the most intense period (in mm),
- intensity of precipitation during the most intense period (in mm h^{-1}).

The average duration of these precipitation systems (*Table 1*) was 6.2 h. In addition to overall statistics, we also investigated mesoscale precipitation systems with an average lifetime of 1 to 6 h. However, due to limitations of the recordings available to us, we were not able to delineate the precipitation cores embedded in synoptic-scale systems in every case. The primary reason for this was the complicated nature of the precipitation fields during many frontal passages. Consequently, we had to reduce the number of cases further by excluding precipitation events that lasted more than 6 h and thus were likely produced by processes operating at scales larger than the convective or meso scales.

Table 1. Heavy rainfall characteristics for Hungary based on 93 cases, 1985-89

Cases	All (n=93)	Duration <6 h (n=58)
Entire system		
Lifetime (h)	6.2	2.5
Precipitation amount (mm)	24.9	20.0
Lifetime average precipitation intensity (mm h^{-1})	8.6	12.0
Most intense period		
Lifetime (min)	7.4	6.7
(h)	0.12	0.11
Precipitation amount (mm)	4.8	5.8
Maximum precipitation intensity (mm h^{-1})	48.0	61.0

It is apparent from Table 1 that shorter system lifetimes result in reduced amounts of total precipitation over the lifetime of the entire system; however, the corresponding precipitation intensity increases significantly. This is also true for the most intense precipitation period within the system. For mesoscale systems lasting less than 6 h, ~30% of the total amount of precipitation comes from the most intense period of the event, in spite of the fact that this period is only about one-twentieth of the entire system lifetime.

An examination of the frequency of precipitation system start times (*Table 2*) reveals that 41% of the events lasting under 6 h begin during the afternoon convective time period between 3 and 5 PM LST, while 19% begin sometime in the 8-h time period between 4 AM and noon LST. If we select cases with core precipitation amounts in excess of 50 mm, the most dangerous 18 events, instead of the 60% during these two time periods for the full set, 72% of the events now develop during these two periods of the day. (Note that this latter percentage is in fact understated given that the morning period for the latter events is two hours shorter.)

Table 2. Diurnal variation of heavy rainfall in Hungary based on 58 cases during 1985–89 with duration <6 h

Cases	All (n=58)	Precipitation amount >50 mm (n=18)
Time of day (LST)	19%	
04:00–12:00		22%
05:00–11:00		
15:00–17:00	41%	50%
Total	60%	72%

The rain events described in this paper are each part of larger synoptic weather patterns. Might they also be part of an MCC, as defined for the largest organized mesoscale convective systems (*Maddox*, 1980)? The occasional occurrence of MCCs or the more generic MCS in the Carpathian Basin is suggested by *Bodolai-Jakus et al.* (1987), who describe heavy rainfall events in Hungary and the Carpathian Basin with features that resemble those in MCCs.

MCCs are defined by the size, shape and duration of the cloud as seen in a thermal infrared satellite image. These large organized convective clouds must attain the criteria outlined in *Table 3*. Consequently, these systems are more than two orders of magnitude larger than individual thunderstorms. Their cousins, the MCSs, have similar characteristcs, but are smaller and last for shorter times.

Table 3. Definition of mesoscale convective complexes (MCC) based on analyses of enhanced IR satellite imagery*

Size†	A. Cloud shield with contiguously low IR temperature $\leq -32°C$ must have an area 100,000 km^2 B. Interior cold cloud region with temperatures $\leq -52°C$ must have an area $\geq 50{,}000$ km^2
Duration	Size definitions A and B must be met for a period of $\geq 6h$
Maximum extent	Contiguous cold cloud shield (IR temperature $\geq -32°C$) reaches maximum size
Shape	Eccentricity (minor axis/major axis) must be ≥ 0.7 at the time of maximum extent

* After *Maddox*(1980)

† Initiation occurs when size definitions A and B are first satisfied. Termination occurs when size definitions A and B are no longer satisfied.

The results of Tables 1 and 2 are in a similar vein. Since one characteristic of MCC precipitation is a tendency for maxima in the few hours after local midnight, the tendency shown in the tables toward increasing rainfall during the early morning hours for the most intense events is at least indicative of mesoscale development. To further address this possibility, we have computed regional statistics for precipitation totals for 6 h diurnal periods during the summer of 1997 using rainfall reports from reporting stations in four regions of Hungary (*Fig. 1)*. In all regions (with the exception of the mountainous region of northeast Hungary, where orographic processes tend to dominate), there are maximum precipitation rates in the early morning hours between 00:00 and 06:00 UTC. Diurnal differences are strongest in southeast Hungary. Precipitation frequencies, on the other hand, have the familiar afternoon thunderstorm maxima in all regions (not shown).

Although these overall statistics are consistent with MCC development, the case presented here provided no clear evidence of MCCs in the satellite imagery or other observations. Furthermore, examination of satellite and radar observations in the region of several other severe precipitation events during the summers of 1997 and 1998 did not definitively identify MCC development, although smaller mesoscale systems did undoubtedly occur.

Development of very large MCSs or MCCs in the Carpathian Basin may be limited by several factors. Probably the most compelling is the lack of a continuous low-level moisture supply. A related factor involves the existence of raised terrain on all sides of the Basin, which does not lend itself to the development of a strong low-level jet of the kind that appears to be a critical

component of United States MCCs. The only exception is the Southwest, where the warm moist air from the Mediterranean can more easily reach the Basin. Thus, although MCSs and possibly MCCs may form in the Basin, they are likely to be less frequent and usually smaller and shorter lived than the MCCs in the United States, where the terrain is ideal for their development.

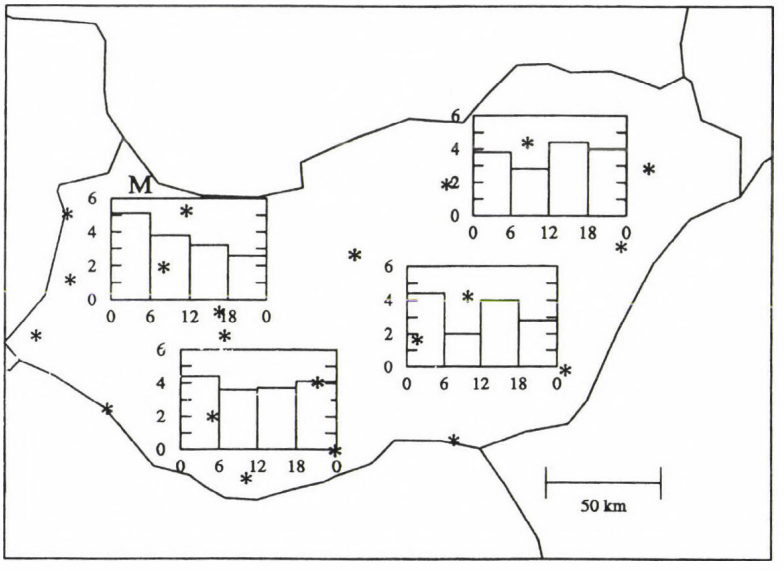

Fig. 1. Diurnal variation of precipitation in four regions of Hungary observed at gauge sites (denoted by asterisk) measuring 6 h precipitation totals. Times along the x-axes are in UTC. Precipitation values (mm) along the y-axes are averaged over all available nonzero observations during June–August 1997. The location of Mosonmagyaróvár is indicated by "M".

3. Possible maximum precipitation method

3.1 General description of precipitation systems

Systems that produce very heavy precipitation in a short period of time are among the most dangerous mesoscale weather phenomena. Although system lifetimes typically vary between 1 and 6 h, they are occasionally as short as 10 to 30 min. Their areal extent is on the order of 10 to 100 km. Frequently these systems cannot be observed with conventional meteorological instruments, making their prediction impossible. Because remote sensors like radar and

satellites provide quasi-continuous measurements in space and time, they allow the identification and tracking of these systems during development and later in their lifecycle. These platforms thus provide a basis for prediction, but only for a relatively short lead-time ranging from 0 to 2 h (*Browning*, 1982). Consequently, this type of prediction serves mainly as a means for issuing watches and warnings.

If we wish to study precipitation systems that produce heavy rainfall in a short period of time over a small area, we need to examine all physical processes that play a significant role in producing precipitation. The basic conditions for creating precipitation in the atmosphere (*Harvey*, 1976) are:

- sufficient moisture content,
- cooling of air to its dewpoint (saturation),
- condensation,
- growth of raindrops.

Because in most cases air cools as a result of upward motion, it is very important to examine vertical motion processes. Heavy rainfall develops under conditions of upward vertical motions that exceed those for other precipitation systems by an order of magnitude. Therefore, for the development of intense precipitation systems we need to consider convective ascent, and because this ascent results from the instability of the air column, we need to assess atmospheric instability also.

In almost every case where the above conditions are satisfied, precipitation occurs; however, the precipitation magnitude will not always be large. Consequently, beyond satisfying these conditions, it is important to examine how physical processes change during severe precipitation systems (*Takács*, 1989).

We can examine the physical processes involved in precipitation formation through the parameters describing them. The precipitable water (W_p) is the most appropriate parameter for calculating the moisture content of the atmosphere. This represents the liquid water content that would result from condensation of all water vapor in the atmosphere. It can be calculated for the layer between any two pressure surfaces by using the computational algorithm of *Schlatter* and *Baker* (1981).

The extent of saturation can be expressed by the dynamical saturation deficit (RT–RT_t), given here as the difference between the actual thickness (RT) and the saturation thickness (RT_t) between any two pressure surfaces. The calculation is again performed by using the computational algorithm of *Schlatter* and *Baker* (1981).

In quantitative precipitation forecasts the precipitable water and the saturation deficit are generally determined for the layer between the 1000 and 500 hPa pressure surfaces. For our study, it turned out to be very helpful to calculate these parameters for several layers, including those between 1000 and 925, 925 and 850, 850 and 700, and 700 and 500 hPa. Multiple layers were

useful because during periods of intense precipitation moisture parameters like those studied here behave in a dissimilar fashion within the different layers.

We estimated the extent of lifting by using the vertical velocity at the 850 hPa, a level near the middle of the lowest 3 km of the troposphere (*Bodolainé*, 1983). To determine the total lifting during 12 hour periods, we used a regression relation between the isallohyptic field and the vertical velocity calculated from the wind field by the kinematic method.

To approximate atmospheric stability we first applied the well-known Showalter (*SSI*), *K* and *NI* indices in the manner described by *Makainé* and *Tóth* (1978). Because these indices were not sufficient to delineate heavy rainfall situations, we added the Total Totals (*TT*), Vertical Totals (*VT*), and Cross Totals (*CT*) instability indices used by forecasters in the U.S. (*Maddox*, 1979). Definitions of these indices are listed in *Table 4*.

Table 4. Stability indices

Showalter index (SSI)	SSI	$= T_{500} - T_{500Parcel}$
K index (K)	K	$= (T_{850} - T_{500}) + (T_{d850}) - (T_{700} - T_{d700})$
NI index (NI)	NI	$= (T_{850} - T_{d850}) + (T_{700} - T_{d700}) + (T_{500} - T_{d500})$
Total Totals (TT)	TT	$= (T_{850} + T_{d850}) - 2T_{500}$
Vertical Totals (VT)	VT	$= T_{850} - T_{500}$
Cross Totals (CT)	CT	$= T_{d850} - T_{500}$
	where	T_{850} is 850 hPa temperature
		T_{700} is 700 hPa temperature
		T_{500} is 500 hPa temperature
		$T_{500Parcel}$ is lifted parcel temperature at 500 hPa
		T_{d850} is 850 hPa dewpoint temperature
		T_{d700} is 700 hPa dewpoint temperature
		T_{d500} is 500 hPa dewpoint temperature

The condensation level and the expected height of the cloud tops were used to estimate the size of the cumulonimbus storm clouds. We used hand analysis methods to deal with phenomena that cannot be easily parameterized. These included specific configurations of pressure and temperature, high- or low-level jets, and areas with wind speeds exceeding the surrounding environment.

3.2 Estimating the location of heavy convective rainfall

To correctly estimate and apply the parameters that describe precipitation-producing physical processes for heavy rainfall forecasting or warning, we need to understand their behavior when such precipitation systems occur. For this part of the study, we used the same 93 cases for which heavy precipitation

statistics were described in Section 2. We determined the average value of all parameters in our set of heavy precipitation cases and used these averages as first approximations to parameter thresholds.

With these thresholds in mind, it is possible to determine regions with the highest likelihood of heavy rainfall by overlaying analyzed parameter fields on a composite chart and locating common areas where the individual parameters exceeded or closely approached their thresholds. Analyses were performed using sounding data at times closest to the time of interest. *Fig. 2* shows a composite chart where this common area is clearly indicated and where heavy precipitation did in fact occur. (We have plotted only three parameters in the figure for ease of visualization.)

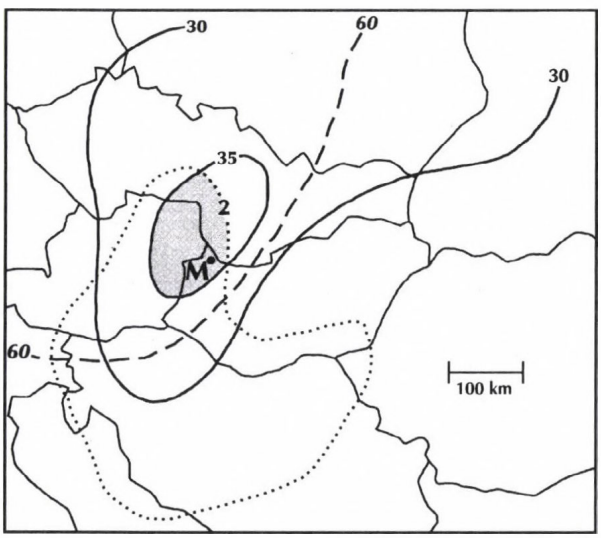

Fig. 2. Composite chart produced from observations at 00:00 UTC on 28 July 1998. The dotted contour encloses SSI values smaller than 2, solid contours are W_p in units of mm, and the dashed contour encloses RT–RT_t values smaller than 60 gpm. Within the shaded area all parameters exceed threshold values. "M" denotes the location of measured rainfall of 132 mm at Mosonmagyaróvár.

Conventional meteorological observing systems do not lend themselves to the determination of the time of initiation of precipitation. To do this, we need meteorological radar and satellite measurements, preferably in digital form. Because the main objective of our paper is to improve our ability to estimate and forecast the amount of heavy rainfall, we do not directly consider the issue of convective initiation.

3.3 Estimating the magnitude of heavy rainfall with the PoMP method

In our experience, numerical forecast models generally underestimate the magnitude of extreme precipitation events. Therefore, our main goal is to demonstrate a method suitable for estimating the actual amount of precipitation for situations in which very large amounts can be expected.

Our method is based on the Probable Maximum Precipitation (PMP) estimation technique. Conceptually, the PMP is the greatest depth of precipitation that is physically possible for a given storm area and duration (*Hansen et al.*, 1982). This value will vary with geographical location and time of year.

In actual atmospheric situations, the PMP will be impossible to achieve because of atmospheric constraints on the production of rainfall. Thus, the PMP will be an unrealistically large estimate. We hypothesize, however, that if the PMP exists and can be accurately determined, then it can also be used to provide an upper limit of precipitation potential for actual atmospheric situations. For the sake of distinguishing it from the Probable Maximum Precipitation, we designated this more restricted estimate the *Possible* Maximum Precipitation, or PoMP.

One method to estimate the PoMP is to maximize the individual components of the formula used to calculate the precipitation amount P (mm/12 h):

$$P = \frac{W_p w}{RT - RT_t}, \tag{1}$$

where

W_p = potential precipitable water (mm) between 1000 and 500 hPa levels;
w = vertical velocity (gpm/12 h) at the 850 hPa level; and
$RT - RT_t$ = dynamical saturation deficit (gpm) between 1000 and 500 hPa levels. (This formula is part of the Meeting Model which is used operationally for quantitative precipitation forecasts at the HMS; see *Bodolainé*, 1983).

Similar to our earlier studies (Section 3.2), we use average component values computed from case studies as thresholds when the computed components are less than these averages. However, when the actual computed values are larger than their thresholds, we use those instead. We remark here that in the case of W_p, the value computed for the layer between 1000 and 500 hPa levels results in good estimates for P. By the same token, the dynamical saturation deficit in either of the two lower layers (between 1000 and 925, or 925 and 850 hPa) provides a better estimate of heavy rainfall amount. This suggests that for the occurrence of extreme precipitation it is necessary to have high moisture content throughout the entire air column, while saturation in lower layers is sufficient to satisfy the condition of heavy rainfall.

By performing the estimation for all radiosonde stations, we obtain a precipitation field which shows the possible maximum values at all points. In reality, of course, these values will never occur simultaneously over the entire field. However, we hope that at any given point the PoMP will provide forecasters with a satisfactory first-guess estimate of precipitation amount in case extreme rainfall does in fact occur. The estimation can be performed after each radiosonde measurement, so that in practice we can have a newly estimated field every 12 h.

We performed an experiment on an independent sample of rainfall events (not shown), which indicated 67% agreement between the PoMP prediction of heavy rainfall and actual events. We consider this good result to be a partial confirmation of this method. We believe that the results can be further improved if we consider hourly surface measurements and, in particular, radar and meteorological satellite measurements to periodically correct the first-guess field.

4. Satellite rainfall estimates

4.1 The Griffith-Woodley technique

The Griffith-Woodley satellite rain estimation technique is an empirical scheme originally developed for estimating convective rainfall in the subtropics (*Griffith et al.*, 1978) and the tropics (*Woodley et al.*, 1980; *Augustine et al.*, 1981). The technique involves several assumptions. First is that convective clouds, whether they are observed on satellite images or as radar echoes, follow a life cycle during which rain amount increases to some peak amount, then drops off as the cloud rains out and the visual cloud dissipates. The technique also assumes that the amount of rain produced varies with the size of the cloud—bigger clouds, as well as clouds with colder tops, produce more rain than their smaller, warmer cousins.

The technique uses a sequence of digital, thermal infrared satellite images to compute rainfall automatically. In deriving the technique, convective clouds were identified on the Synchronous Meteorological and Geostationary Operational Environmental Satellite (SMS/GOES) thermal infrared images, and were calibrated with a combined system of WSR-57 (10-cm S-band) weather radar data and hourly rain gauge data from a dense network (1 gauge per square mile) in south Florida, USA. Since not all clouds produce rain, a study was performed to determine the temperature that identifies raining clouds with the result that raining clouds are defined to be those clouds that are −20°C or colder, and it is this temperature that determines the area of the cloud. Rain volume (R_v) is estimated for each cloud as a function of the size of the cloud, the cloud-top temperature, and whether the cloud is increasing or decreasing in size:

$$R_v = I \cdot < A_e/A_m > \cdot A_m \cdot \Delta t \cdot \sum [a(i) \cdot b(i)] \cdot 10, \quad (2)$$

where

R_v is rain volume for a single cloud (m^3),
I is rain rate (mm h^{-1}) derived from radar echo data,
A_e is radar echo area (km^2),
A_m is maximum area during a cloud's lifetime (km^2),
$< A_e/A_m >$ is an inferred coverage of the radar echo area for the cloud,
Δt is the time interval between successive satellite images (h),
the *summation* produces more rain for clouds with tops colder than –20°C,
a is the fractional coverage of the cloud for temperatures colder than –20°C,
b is an empirical weighting coefficient that increases rainfall for clouds colder than –20°C,
and the *factor* of 10 accounts for conversion among units.

The period of the rain is the time of the image forward to the time of the next image. Thus, if satellite images are at 30-min intervals, the calculated rain represents rain ending 30 min after the image time. The value of the coefficient b is computed from

$$b = \exp(0.02667 + 0.01547D)/11.1249 \qquad 154 \leq D < 176, \quad (3a)$$

$$b = \exp(0.11537 + 0.01494D)/11.1249 \qquad 176 \leq D \leq 255, \quad (3b)$$

where

D is digital count from the GOES IR image.

Rain volume is not the usual variable; rainfall amounts are typically reported and displayed. Consequently, a scheme to derive isohyets, referred to as the "10/50–40/50" apportionment scheme, has been devised. The scheme is named the "10/50–40/50" apportionment because it apportions half of the total rain volume to the coldest 10% of the cloud ("10/50"). The remaining 50% of the rain volume is apportioned to the other half of the cloud, that is, to the second coldest 40% of the cloud ("40/50"). The motivation for this is the following. The –20°C temperature contour is used to identify raining clouds, to calculate cloud area, and to compute the volume estimate, but we know from studies performed during the technique's calibration that rain does not fall under the entire –20°C area. In growing and mature systems, the overshooting tops are the coldest part of the cloud, and represent its most active part. Thus, we attribute the active rainfall area to only the coldest half of the cloud, and make rain amount a function of cloud-top temperature as well. To compute rain amount, cloud-top temperatures are ranked coldest to warmest, and pixels in the coldest 50% have the following amount of rain:

$$D_{i,j} = \{[(R_v/2) \cdot b_{ij}]/(g_{ij} \cdot \Sigma b)\} \cdot 10^{-3}, \quad (4)$$

where

$D_{i,j}$ is rain amount (mm) in the satellite i,j pixel,
$R_v/2$ is one-half of the cloud's rain volume (m^3) on a particular image,
b_{ij} is the empirical weighting coefficient for the i,j pixel,
g_{ij} is the area (km^2) of the i,j pixel,
the sum is over the coldest 10% (or second coldest 40%) of the pixels, and the factor of 10^{-3} converts among units.

Although the Griffith-Woodley rain estimate technique was derived for tropical and semi-tropical situations, the technique was modified to work in the midlatitudes by accounting for environmental differences between Florida and the location of interest. The underlying assumption is that the dynamical processes of convective clouds are similar no matter where they occur, but that it is differences in moisture in lower levels, entrainment at midlevel, and cloud height and horizontal extent that produce differences in rainfall amount. *Griffith et al.* (1981) used a one-dimensional cumulus cloud model (*Simpson* and *Wiggert*, 1969; 1971) to correct for these differences. Mandatory- and significant-level data from an atmospheric sounding are input for the 1-D model. The model performs a single-sounding analysis, computing cloud base, cloud top, and precipitation production, using Kessler's cloud physics scheme for 8 thermal bubble sizes, ranging from 500 to 3,000 m. Model output consists of cloud-top height (m), and cloud water (g kg^{-1}).

Because the appropriate bubble radius is not known *a priori*, the average *(Rbar)* and standard deviation *(σ)* of the model-predicted cloud water of the 8 bubbles are computed each time a sounding (or pseudo-sounding) is run. An environmental correction factor, the model adjustment factor *(MAF)* is computed from the average and standard deviation:

$$MAF = (Rbar \cdot \sigma)/(Rbar_F \cdot \sigma_F), \quad (5)$$

where $Rbar_F$ and σ_F are the mean and standard deviation based on an average Florida sounding. The values of $Rbar_F$ and σ_F are 10.210 g kg^{-1} and 4.195 g kg^{-1}, respectively. A sample output from the 1-D cloud model and *MAF* computation is shown in *Table 5* for an Aladin pseudo-sounding from Budapest. Since this sounding produces cloud water values that are smaller than the average values for Florida, the estimated satellite rainfall for this region is reduced by a factor of 0.51.

Model adjustment factors are computed at every sounding location available at a given time. The *MAFs* are interpolated to the satellite grid using a Barnes interpolation scheme (*Barnes*, 1964) to produce a field of model adjustment

factors. The gridded satellite estimates are multiplied by this 2-D field of *MAF*s to produce an environmentally corrected rain estimate.

Table 5. 1-D cloud model output for the 21:00 UTC Aladin pseudo-sounding for Budapest, Hungary on 27 July 1998

Radius (m)	Cloud water ($g\ kg^{-1}$)
500	1.133
750	3.711
1000	5.818
1250	8.004
1500	8.539
2000	9.177
2500	9.584
3000	9.865
Average	6.979
σ	3.154
MAF	0.51

4.2 Modifications for operational use at HMS

The FORTRAN code for the Griffith-Woodley technique with several modifications was transferred for use in Hungary. The first modification was to translate between METEOSAT and GOES digital counts. For both GOES and METEOSAT, counts range from 0 to 256. However, GOES counts are inverted (cold tops have high counts, warm tops have low counts) compared to METEOSAT data. A relationship between METEOSAT counts and brightness temperature was provided by the Satellite Laboratory of the HMS for 6 and 7 July 1997, and from this relationship a second-order polynomial was fit to the GOES and METEOSAT data. METEOSAT counts are converted to equivalent GOES counts before the rain computation is done.

A second modification was to use the so-called streamlined version of the technique. Eq. (2) describes the life history technique, which is a diagnostic technique. Before a calculation of a cloud's rainfall can be computed, a sequence of images showing a relative maximum in cloud area must be in hand. The life history technique clearly cannot make estimates in real time. The streamlined version remedies this by assuming a fixed value of 16.7×10^2 mm h^{-1} for the rainfall rate, I. The echo coverage ratio ($<A_e/A_m>$) also assumes a fixed value which varies with the size of the cloud—0.067 for clouds larger

than 10,000 km^2, 0.047 for clouds between 2,000 and 10,000 km^2, and 0.016 for clouds smaller than 2,000 km^2. Eq. (2) then becomes

$$R_v = C \cdot A_m \cdot \Delta t \cdot \Sigma[a(i) \cdot b(i)] \cdot 10, \tag{6}$$

where C is 26.72, 78.49, or 111.89 depending on cloud size as noted above, and, unlike Eq. (2), A_m is cloud *area* measured on the picture of interest, not maximum area. The other terms are as defined before.

Third, twice daily operational sounding data are usually used to calculate the model adjustment factor. At the HMS, we tested the suitability of pseudo-soundings available every three h from the Aladin model (*Horányi et al.*, 1996). This meant that model adjustment factors were updated every 3 h using the model data, rather than every 12 h from the temperature (i.e., sounding) data. Also, pseudo-soundings can be generated from the model for any location where extreme rains are possible. Thus PoMP no longer has to be dependent on the operational soundings in a small number of locations.

Last, at the time of the study operationally available satellite data at the HMS consisted of two types: digital data that are transmitted every three hours, and digitalized METEOSAT images at 30-min intervals filling the gap between the digital images. We decided to use both the digital and digitalized images in the rain computation in order to have a more complete record of the temporal evolution of the clouds. The implications of this are discussed below.

5. Case study

5.1 Synoptic situation

On 27 and 28 July, 1998, a relatively slow-moving, active cold front passed over the Carpathian Basin (*Fig. 3*). Ahead of the front on the 27th, a warm, very moist air mass moved into the warm sector, raising maximum temperatures over most of Hungary above 30°C. On that day, severe thunderstorms initially developed in the warm sector over the Kisalföld region of Hungary, later spreading into the eastern half of the country. Substantial precipitation (20–30 mm) fell in the northwest; in Mosonmagyaróvár an impressive 132 mm was measured during a 1.5 h period between 2300 UTC on 27 July and 0100 on 28 July (*Fig. 4*). Hail was also observed here.

The following contributed to the heavy precipitation:

- the large amount of precipitable water (32–35 mm);
- near-saturation atmospheric conditions (<60 gpm);
- surface wind convergence;
- the development of significant temperature contrast and wind convergence at the 850 hPa level; and
- an area of higher windspeed at 500 hPa (>25 m s^{-1}).

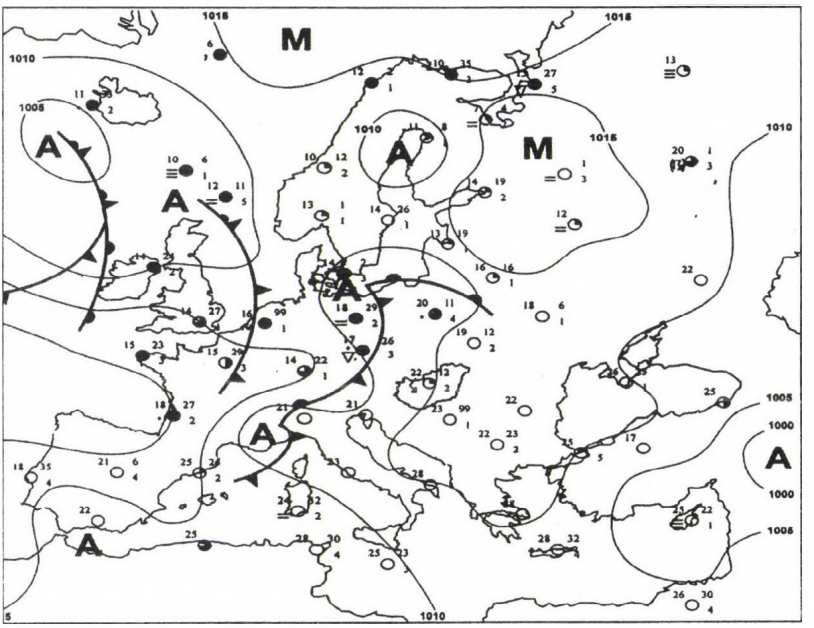

Fig. 3. Synoptic map for 00:00 UTC 28 July 1998 provided courtesy of the Hungarian Meteorological Service.

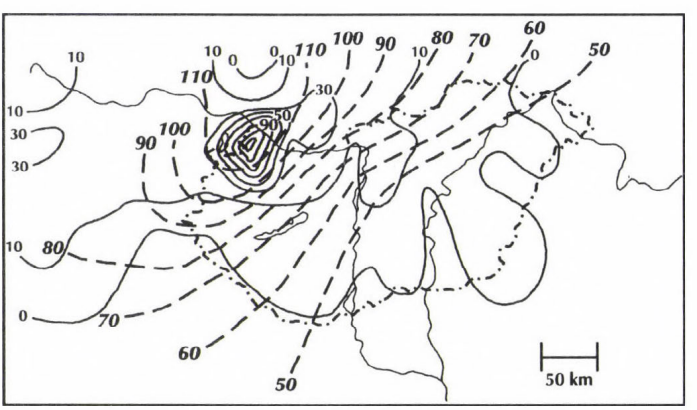

Fig. 4. PoMP (mm) for 00:00 UTC 28 July 1998 (dashed contours) and precipitation (mm) observed between 06:00 UTC 27 July and 06:00 UTC 28 July (solid contours).

5.2 PoMP results

Using parameters that describe the above-mentioned phenomena, a composite chart (Fig. 2) was created from 00:00 UTC 28 July radiosonde observations. From the chart, it is possible to delineate a high-risk area within which severe local precipitation may occur. Estimates of this area given by the PoMP computed by the previously described method are shown on Fig. 4. In this case, the method worked quite well; it is apparent that both the location of the precipitation maximum and its magnitude were accurately estimated.

5.3 Satellite rainfall estimates

Satellite estimates for each day during summer 1998 were computed in near real time using the digital plus the digitalized METEOSAT imagery. These results will be referred to as the D+D set. In general, the satellite estimated rainfalls were too large compared to the gauge amounts, and the areal extent of the satellite rains seemed to be greater than indicated by the gauge data. A statistical comparison of satellite and gauge amounts for the 24-h period ending at 06:00 UTC 28 July 1998 bears this out. For this comparison, the half-hourly satellite estimates were bilinearly interpolated to gauge locations, and then summed. Point comparisons are made for the operational gauge data from the Carpathian Basin. Gauge data have been provided by the Meteorological Service of the Hungarian Republic, and the national weather services of neighboring countries.

The average D+D satellite estimates are much larger than their gauge counterparts (31.4 vs. 7.9 mm) and have greater standard deviations (52.8 vs. 15.2 mm) (see *Table 6*). Median values for the gauge and satellite data sets are very small (0.8 and 0.0 mm, respectively) because of the large number of reports of no rainfall for this day. Approximately one-third of the gauges and about half the satellite estimates are zero. When the zero values are removed (see the lower half of Table 6), the satellite average and median values (65.0 and 51.3 mm, respectively) are five to six times larger than the gauge average and median values (12.2 and 8.8 mm, respectively). The bias (defined as the satellite estimate less the gauge amount) and root mean square error (defined as the square root of the average of the squared bias) are also very large, being 23.5 and 53.7 mm, respectively.

A plot of these 112 points (*Fig. 5*) shows that the data are widely scattered with low correlation (0.41). Satellite rainfalls are more likely to overestimate the gauge rainfalls than to underestimate them. For the two satellite outliers at small gauge rainfalls, the satellite estimates (which are on the order of 250 mm) are a factor of 10 greater than the gauge amounts (which are on the order of 20 mm). The heaviest rainfall of 132.1 mm occurred at Mosonmagyaróvár. Storm total rainfall from the satellite estimate in the four pixels surrounding this

gauge have values of 60.8, 72.6, 104.4, and 130.2 mm. The interpolated satellite amount is 85.7 mm, about one-third smaller than the actual amount.

Table 6. Sample statistics for 24 h accumulated rainfalls ending 06:00 UTC 28 July 1998

	D + D	Gauge	DO
Number	112	112	112
Average (mm)	31.4	7.9	25.7
Standard deviation (mm)	52.8	15.2	52.0
Median (mm)	0.0	0.8	0.0
Bias (mm)	23.5	-	33.6
RMS error (mm)	53.7	-	51.2
No. non-zeros	54	72	45
Average (mm)	65.0	12.2	63.9
Standard deviation (mm)	76.4	19.0	82.6
Median (mm)	51.3	8.8	36.3
Bias (mm)	36.0	-	54.5
RMS error (mm)	66.5	-	63.5

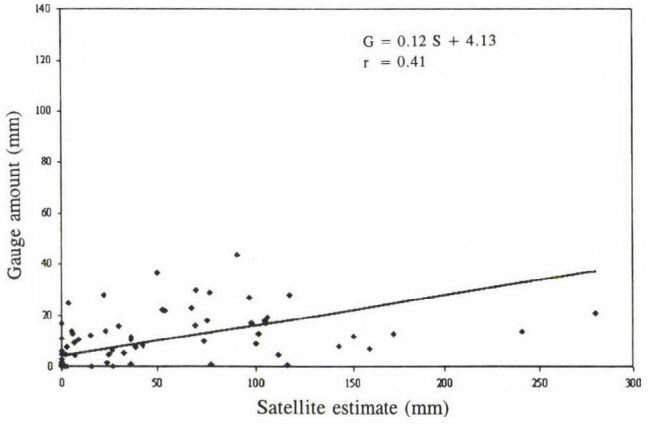

Fig. 5. Scatterplot of the satellite estimates from the digital plus digitalized data set for the images between 09:00 UTC 27 July 1998 and 06:00 UTC 28 July 1998, and their corresponding gauge amounts for the 24 h period ending 06:00 UTC 28 July 1998. The regression fit and correlation coefficient are also shown.

There are several reasons why satellite estimates and gauge observations should differ. The most obvious is that satellite estimates represent rain amounts averaged over much larger regions than the gauge rainfalls. A satellite pixel nominally represents ~ 50 km^2. In convective rains, gauge amounts may be representative of only 10 km^2 or less. Consequently, satellite amounts should be expected to underestimate peak rainfalls for convective systems. This has been found in previous verification studies (*Griffith et al.*, 1978; *Augustine et al.*, 1981; *Griffith et al.*, 1981; *Griffith*, 1987). However, in this study overestimation by the satellite was more likely to occur.

RMS errors between satellite and gauge amounts of 50 to 70 mm are much larger than those seen in a previous summertime application of the technique (*Griffith*, 1987), where rms errors for daily point rainfalls were about 15 mm. (Correlations were comparable.) It was suspected that the digitalized imagery was a source of error in the rain estimates. There are large differences between the appearance of clouds in the digital and digitalized images. The digitalized images appear to have a smaller range of brightness, and the clouds look fuzzier. The rainfall patterns (*Fig. 6*) are dramatically different. Thirty-minute rainfalls computed from a digital image (*Fig. 6a*) are fairly smooth, whereas those computed from the digitalized image (*Fig. 6b*) have many centers of rain maxima. It is unlikely that the cloud has changed this drastically in 30 minutes. In fact, there is always a similar looking discontinuity in the isohyets between every pair of digital and digitalized images. These localized bright spots in the digitalized data produce overestimates in the satellite rains.

The drawback of the digital data set is that these images are available only every 3 hours. The effect of infrequent images is also toward overestimation. In the technique, cloud top temperatures are assumed to be static between images. This assumption is obviously not true, but it's not too bad an assumption for time periods short compared to the life time of the cloud. However, when there are no more frequent images then every three hours, and the growth or decay of the cloud is not updated, the computed rain that is extrapolated from this single image is generally too great compared to the actual rain falling in the subsequent three hours.

Nevertheless, to test the effect of the digitalized data, satellite rainfalls were estimated using only the digital images (DO). *Fig. 7* is a scatterplot of estimated rain amounts from the DO imagery versus gauge amounts. Average values and standard deviations of the satellite estimates (Table 6) are still much larger than the gauge values, but less than the estimates for the D+D data. The satellite-estimated rainfall at Mosonmagyaróvár has increased significantly (to 112 mm, interpolated from 17.3, 67.2, 68.7, and 194.3 mm), but so have the estimated rains for the two outliers in the upper right-hand corner of Fig. 6. These now exceed 270 mm.

One last meteorological factor needs to be addressed. While there is convection on this day, it is embedded in the front. The Griffith-Woodley rain

estimation technique was derived for free convection, and its most successful applications are for isolated convective systems. In an unpublished study of the application of this technique to embedded convection ahead of fronts in the United States during the winter, we found poor comparisons between the satellite and gauge results.

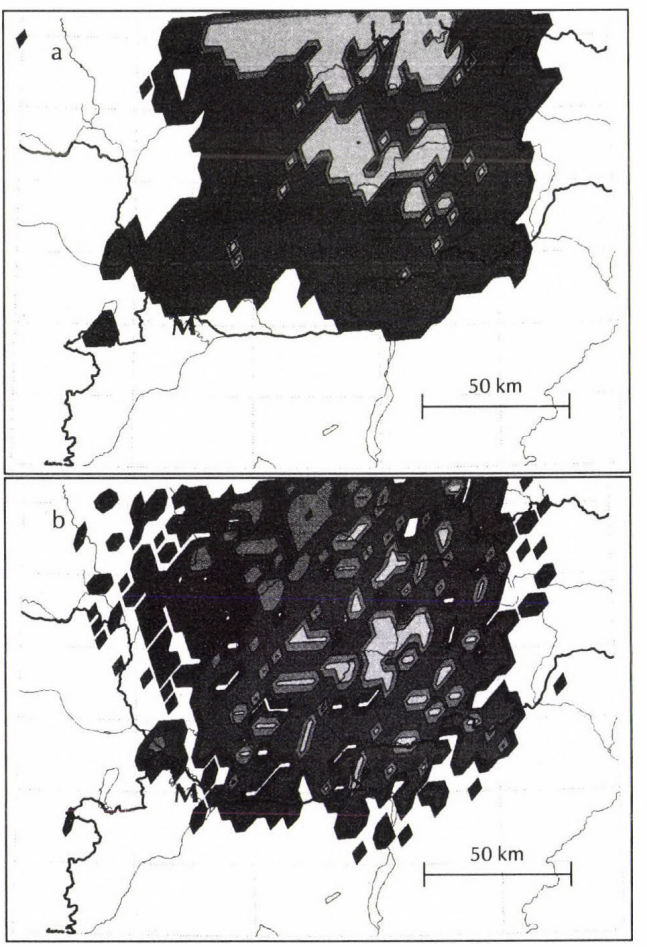

Fig. 6. Satellite estimates of 30-min rainfall on 27 July 1998 (*a*) at 21:00 UTC for a digital and (*b*) at 21:30 UTC for a digitalized image. Rainfall contours are 0–5 mm (dark grey), 5–10 mm (medium dark grey), 10–20 mm (medium light grey), and >20 mm (light grey). The heavy solid line running horizontally across each panel is the border between Hungary and the Slovak Republic. The location of Mosonmagyaróvár is indicated in each panel by "M".

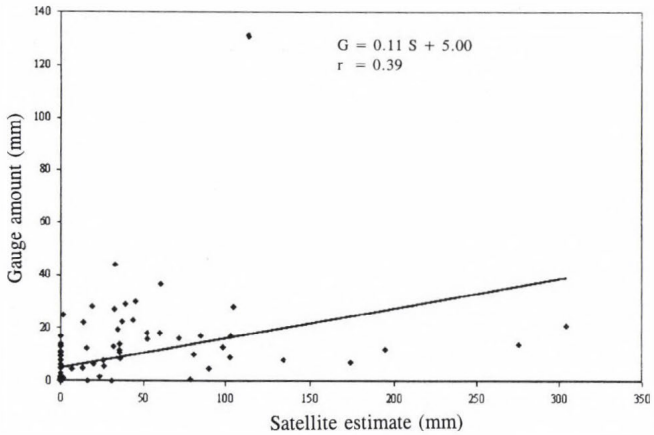

Fig. 7. Same as *Fig. 5*, but for the digital only (DO) images between 09:00 UTC 27 July 1998 and 06:00 UTC 28 July 1998.

6. Conclusions

The success of the PoMP method in delineating regions of heavy precipitation in the case study presented here suggests that it can be used to provide a first-guess estimate for the amount of heavy rainfall during episodes of large precipitation. These estimates are likely to be more realistic than precipitation output from numerical weather prediction (NWP) models, which tend to underestimate rainfall in these situations. Operational runs of the satellite rain estimation technique timed to update the PoMP fields during potentially serious rainfall episodes could add critical lead time to heavy rainfall warnings. This would be particularly true if soundings from NWP models like Aladin were used to produce the necessary map adjustment factors at times that are several hours removed from synoptic radiosonde observations. Ultimately, the hope is to provide warnings that are more timely and more accurate, and thus more likely to save lives and property.

For the Mosonmagyaróvár case and two others not shown, satellite rain estimates from the D+D imagery overestimated the rain measured by the gauges in the mean, and underestimated the maximum rainfall at the location of the event. The overestimation appears to be caused in part by use of the digitalized imagery. For the maximum gauge amounts, the satellite appears to have underestimated rain because of the relatively coarser resolution of the satellite pixels and the bilinear interpolation of the satellite data to gauge location. In fact, individual pixel rainfalls in the vicinity of the gauge locations

could be quite close to the gauge value. Differences between gauge and satellite values did not seem to be related to the model adjustment factor. Use of pseudo soundings from Aladin produced reasonable results for the model adjustment factors, despite the limitation that only the mandatory levels are generated.

Two questions about the rainfall estimates remain unanswered. The error in the DO results arising from the 3-h temporal resolution of the digitized imagery is unknown. Similarly, we also could not adequately assess effects arising from the fact that these systems predominantly consist of embedded convection ahead of fronts, for which the Griffith-Woodley technique is known to perform poorly in the winter.

At the Hungarian Meteorological Service, satellite rain estimates are now computed operationally in near real time, are available to forecasters, and are shown at the daily weather briefing. Since the availability of the digital EUMETSAT imagery every 30 min, the satellite estimates appear to cover smaller areas, and to compare better with the gauge data. Analysis of these newer results awaits further study.

Finally, during the course of our study we have learned more about the nature of heavy rainfall-producing systems from the statistical evaluations of parameter thresholds applied in the PoMP computations and from studies of the nocturnal pattern of Hungarian rainfall. More complete studies of heavy rainfall events would undoubtedly help to make these methods more reliable.

Acknowledgments—We thank *Márta S. Buránszki* and *András Horányi* of the Hungarian Meteorological Service for their help during the course of this project. *Imre Bonta* (also of the HMS) provided important analyses of the synoptic conditions for several of the events studied during 1998. We thank *Woody Roberts* of the Forecast Systems Laboratory and *Dongsoo Kim* of the Forecast Systems Laboratory and the Cooperative Institute for Research on the Atmosphere (CIRA) for their useful comments on an early version of this paper, and *Nita Fullerton* of the Forecast Systems Laboratory for a thorough technical review. *John Osborn* of the Forecast Systems Laboratory prepared figures used in this paper. This project is sponsored by the U.S.–Hungarian Science and Technology Joint Fund in cooperation with the Forecast Systems Laboratory and the Hungarian Meteorological Service under Project 523.

References

Augustine, J.A., Griffith, C.G., Woodley, W.L. and *Meitin, J.G.*, 1981: Insights into errors of SMS-inferred GATE convective rainfall. *J. Appl. Meteor. 20*, 509-520.

Barnes, S.L., 1964: A technique for maximizing details in numerical weather map analysis. *J. Appl. Meteor. 3*, 396-409.

Bodolai-Jakus, E., Kapovits, A., Tänczer, T. and *Pintér, F.*, 1987: Detailed Analysis of a meso- scale convective complex situation in the Carpathian Basin. *Proc. Symp. Mesoscale Analysis & Forecasting*, Vancouver, Canada, ESA SP-282, 345-350.

Bodolainé, J.E., 1983: Synoptic conditions of floods over the Danube and the Tisza River Basins (in Hungarian). Országos Meteorológiai Szolgálat Hivatalos Kiadványai XVI, Budapest.

Bodolainé, J.E., 1997: Conceptual models of mesoscale convective systems in Middle Europe (in Hungarian). *Légkör*, Vol. XLII., No. 4., 10-16.

Browning, K.A. (ed.), 1982: *Nowcasting*. Academic Press, London.

Griffith, C.G., 1987: Comparisons of gauge and satellite rain estimates for the central United States during August 1979. *J. Geophys. Res.-Atmospheres 92*, 9551-9566.

Griffith, C.G., Woodley, W.L., Grube, P.G., Martin, D.W., Stout, J. and *Sikdar, D.N.*, 1978: Rain estimation from geosynchronous satellite imagery — visible and infrared studies. *Mon. Wea. Rev. 106*, 1153-1171.

Griffith, C.G., Augustine, J.A. and *Woodley, W.L.*, 1981: Satellite rain estimation in the U.S. High Plains. *J. Appl. Meteor. 20*, 53-66.

Hansen, E.M., Schreiner, L.C. and *Miller, J.F.*, 1982: Application of probable maximum precipitation estimates - United States East of the 105th meridian. *Hydrometeorological Report*, No. 52. National Weather Service, NOAA, US Department of Commerce, Washington, DC. 168 pp.

Harvey, J.G., 1976: *Atmosphere and Ocean. Our Fluid Environments*. The Artemis Press, Sussex.

Horányi, A., Ihász, I. and *Radnóti, G.*,1996: ARPEGE/ALADIN: A numerical weather prediction model for Central-Europe with the participation of the Hungarian Meteorological Service. *Időjárás 100*, 277-301.

Maddox, R.A., 1979: A methodology for forecasting heavy convective precipitation and flash flooding. *National Weather Digest: Flood 4.*

Maddox, R.A., 1980: Mesoscale Convective Complexes. *Bull. Amer Meteor. Soc. 61*, 1374-1387.

Makainé, Cs.M. and *Tóth, P.*, 1978: *Synoptic meteorology*. Tankönyvkiadó, Budapest.

Schlatter, T.W. and *Baker, D.V.*, 1981: Algorithms for thermodynamic calculations. PROFS Program Office, NOAA ERL. Boulder, CO. (Copy is available from the Forecast Systems Laboratory, R/FS1, 325 Broadway, Boulder, CO 80304-3328.)

Simpson, J. and *Wiggert, V.*, 1969: Models of precipitating cumulus towers. *Mon. Wea. Rev. 97*, 471-489.

Simpson, J. and *Wiggert, V.*, 1971: 1968 Florida cumulus seeding experiment: numerical model results. *Mon. Wea. Rev. 99*, 87-118.

Takács, Á., 1989: Monitoring of weather conditions on mesoscale to improve a precipitation warning system for hydrological purposes. IAHS Third Int. Assembly, Baltimore, MD. *IAHS Publ.* No. 186, 117-123.

Takács, Á., Tollerud, E.I. and *Girz, C.M.I.R.*, 1998: Improving convective forecasts in Hungary. Preprints, *16th Conference on Weather Analysis and Forecasting*, Phoenix, AZ, USA. Amer. Meteor. Soc., 118-120.

Woodley, W.L., Griffith, C.G., Griffin, J.S. and *Stromatt, S.C.*, 1980: The inference of GATE convective rainfall from SMS-1 imagery. *J. Appl. Meteor. 19*, 388-408.

IDŐJÁRÁS

Quarterly Journal of the Hungarian Meteorological Service
Vol. 104, No. 2, April–June 2000, pp. 91–107

Sensitivity of forecast trajectories to wind data inputs during strong local wind conditions

Lazar Lazić[1] and **Ivana Tošić**

Department of Meteorology, University of Belgrade, P.O. Box 368
YU-11001 Belgrade, Yugoslavia; E-mail: lazar@afrodita.rcub.bg.ac.yu

(Manuscript submitted for publication 3 November 1999; in final form 25 February 2000)

Abstract—Forecast reference trajectories and forecast trajectories with different wind data frequencies were computed for two local winds, Bora and Koshawa, at eight vertical levels using Eta Model. 48 h real data simulations of local wind cases were achieved with a 28 km horizontal resolution and 16 layers in the vertical. Numerical experiments with different frequencies of wind data in trajectory calculations (90 s – control case, 15 min, 30 min, 1 h, 3 h, 6 h and 12 h) over the Bora and Koshawa wind regions were performed. These are motivated by theoretically based expectations that a certain intermediate wind data frequency is required for accurate forecast trajectory of downslope and windstorms with Bora and Koshawa wind properties. Three-dimensional forecast trajectories over real mountains with various wind data frequencies were calculated and analysed. The total number of trajectories is 280 in each data set.

Mean absolute error (distance between reference and forecast trajectory), mean relative error (mean absolute error divided by mean reference trajectory for the total transport distance) in both horizontal and vertical directions are computed. The 4515 locations are compared with the control case. The mean relative error for all forecast trajectories is about 30% in Bora case and 20% in Koshawa case. Trajectories with wind data frequency of 15 min, 30 min and 1 h are accurate enough, the mean relative error is less than 10% in Bora case and less than 5% in Koshawa case. The mean relative error of parcel positions along trajectories shows large values in case of 3 h, 6 h and 12 h wind data frequencies, especially in vertical direction. In general, Koshawa case was less sensitive to the temporal frequency of wind data than Bora case.

The maximum of the mean relative error (about 200%) is associated with forecast trajectories in vertical direction in case of 12 h wind data frequency of Bora wind. This result suggests that trajectories calculated from the analysed wind data (12 h data frequency) are not accurate when they are used. This result also indicates the importance of using vertical velocity for calculating trajectories.

Key-words: Eta Model, forecast trajectories, wind data frequency, strong local winds, Bora, Koshawa, mean absolute error, mean relative error.

---

[1] Corresponding author

1. Introduction

Air parcel trajectories have been extensively used over the past decade to study the atmospheric transport because they are relatively simple to compute. An individual trajectory gives only a general description of the flow field. Trajectories can be calculated from observed wind data or wind fields simulated by a numerical model.

The construction of three-dimensional atmospheric trajectories provides a valuable diagnostic tool for illustrating and studying the three-dimensional flow fields, their structure and associated transports, exchange processes associated with extratropical weather disturbances, stratospheric and tropospheric air mass exchanges associated with a jet stream, dispersal of upper atmospheric pollutants and possible nuclear contamination (*Petersen* and *Uccellini*, 1979).

Doty and *Perkey* (1993) examined trajectories in the vicinity of an intense extratropical cyclone using data of various temporal resolutions from 15 min to 12 h. They found small errors (75 km or less) at high-resolution data (15 min to 1 h) and much higher errors (100–500 km) with 3 h data. Regarding the spatial density of data, *McQueen* and *Draxler* (1994) found less error with a higher data density.

Trajectory error may be related to synoptic conditions as well. *Rolph* and *Draxler* (1990) found nearly constant relative error (absolute error divided by forecast trajectory total transport distance), but larger absolute error during cyclonic conditions with strong winds as compared to anticyclonic conditions. *Maryon* and *Buckland* (1995) examined dispersion from a puff released in the atmospheric boundary layer during cyclonic and anticyclonic conditions over ten days with a Lagrangian global multiple-particle model using analysed three-dimensional wind fields. *McQueen* and *Draxler* (1994) found low relative error (15%) with persistently strong flow. *Heffter et al.* (1990) and *Haagenston et al.* (1990) also suggest that relative error is inversely proportional to wind speed.

Local winds Bora and Koshawa are persistently strong flows caused by local orography and specific synoptic conditions. Bora and Koshawa are similar winds (e.g., they are downslope), but there is a difference also. Koshawa is more channelized wind than Bora at larger scales.

The Eta Model (*Mesinger et al.*, 1988; *Janjić*, 1990, 1994) has shown excellent capabilities for simulation of mountain-induced phenomena (e.g., lee cyclogenesis, local winds). Therefore it is expected that the model will also yield realistic trajectories. The trajectory method is a useful tool in displaying and analysing features of the mountain-induced phenomena (*Lazić* and *Tošić*, 1998). This method has previously been used for studying blocking effect of mountains on the atmosphere (*Chen* and *Smith*, 1987).

The purpose of this study is to estimate the forecast trajectory error, using two data sets with strong wind, by comparing calculated trajectories with the control case, which used wind data at the highest available temporal frequency,

that is 90 s in this study. Six experiments used the simulated wind field at smaller temporal frequencies. The first used the wind every 15 min, the second every 30 min, the third every 1 h, the fourth every 3 h, the fifth every 6 h and the sixth every 12 h. Comparisons were made for all trajectories in given horizontal positions (five in this study), all trajectories at given vertical levels (eight in this study), and all trajectories in each data set of Bora and Koshawa.

After presenting general characteristics of the local winds Bora and Koshawa in Section 2, the model summary is given in Section 3, and the scheme for trajectory calculations is presented in Section 4. The error statistics are defined in Section 5. Forecast trajectories with various wind data frequencies are examined in Section 6. The sensitivity of trajectories to the variations of wind data frequencies, using calculated error statistics, are discussed in Section 7. Conclusions are summarized in Section 8.

2. Characteristics of Bora and Koshawa winds

2.1 Characteristics of Bora wind

Bora is a katabatic wind. The kinetic energy of gusts is derived entirely from the potential energy of cold air that spills over the coastal mountain ranges of Dinaric Alps and falls down their steep slopes to the Adriatic Sea (*Fig. 1*).

The Bora occurs when cold air accumulates over the north side of Dinaric Alps. The depth of the cold air reservoir has to reach at least up to the mountain passes for the Bora to commence. Not much movement needs to be present from inland across the coastal mountain ranges, or even at the crest of these mountain ranges, during Bora conditions. The relatively short way of the cold air masses along the mountain slopes is not suffice to warm the descending air to the normal temperatures of the coastal plains. Therefore, Bora is a cold wind.

There are two types of weather patterns which produce the Bora (*Yoshino*, 1976):

- A cyclonic weather pattern (cyclonic Bora) characterized by a depression over the southern Adriatic Sea or the Ionian Sea. Along its southeastern side, warm air is flowing aloft in a southerly to southwesterly air current. Thus the Bora in the lowest layers of the troposphere is overrun by warm, moist air masses.
- An anticyclonic weather pattern (anticyclonic Bora) characterized by strong high pressure over Central Europe, and a not well-developed low to the south.

In each case, the pressure is higher on the continental side of the mountains and lower over the Mediterranean. Therefore, a large horizontal pressure gradient builds up across the mountain barrier of Dinaric Alps.

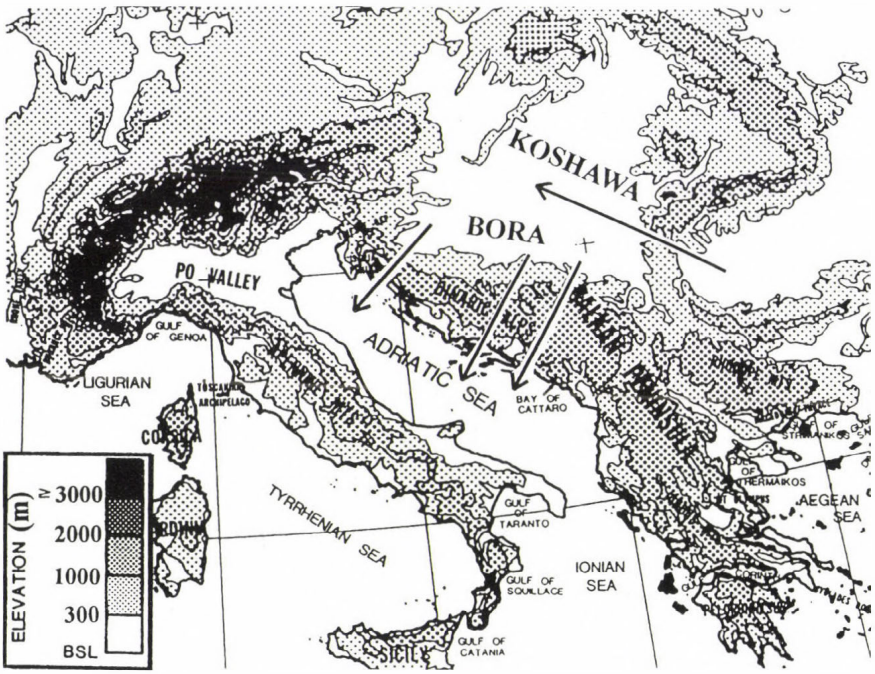

Fig. 1. Bora and Koshawa wind regions with real orography.

Bora is the most common wind in the Adriatic Sea area, where it flows mainly from the northeast through gaps in the Dinaric Alps (Fig. 1). The direction of the wind along the Croatian and Yugoslavian coast depends on the orientation of adjacent mountains, gaps and valleys. Over the open sea, the direction of the Bora is usually northerly to northeasterly, while on the Italian coast the wind almost always backs to a northwesterly direction. Bora is most common during the cold season of the year (November through March).

2.2 Characteristics of Koshawa wind

Koshawa is usually a cold, very squally wind, descending from east or southeast in the region of the Danube "Iron Gate" through the Carpathians (Fig. 1), continuing westward over Belgrade, thence spreading northward to the Rumanian and Hungarian borderlands and southward as far as Nish. In winter it makes the temperature turn as cold as -30°C and it is cool and dusty even in summer. It usually occurs with a depression over the Adriatic and high pressure over southern Russia, which is a frequent situation in winter.

Koshawa is usually explained as a "jet-effect wind" through Iron Gate, giving speeds much above the gradient (*Küttner*, 1940; *Unkašević et al.*, 1999), regarded a katabatic wind, intermediate between foehn and Bora. If the wind is sometimes warm, like a foehn, it is called "warm Koshawa"; if cold like the Bora, it is called "cold Koshawa". The low level jet-effect wind, or low level jet, is a wind which is increased in speed by channeling of the air by some orographic configuration such as a narrow mountain pass or canyon. When air stratification is stable, as it usually is in summer, the air tends to flow through the gap from high to low pressure, emerging as a "jet" with large standing eddies. The excess of pressure on the upwind side is attributed to a pool of cold air held up by the mountains.

The Koshawa has annual variation with a maximum in November and a minimum in July, and it has a marked diurnal variation with a maximum occurring between 05:00 and 10:00 local time.

3. Model summary

The model used for simulation of this study is a limited area primitive equation model with step-mountain coordinate (*Mesinger*, 1984), the so-called Eta Model. The model uses the semi-staggered E grid. The technique preventing grid separation is combined with split explicit time differencing. The horizontal advection has a built-in nonlinear energy cascade control. The internal boundary conditions at the sides of the step-mountains preserve all major properties of horizontal advection. A more detailed description of the dynamical part of the model can be found in *Mesinger et al.* (1988).

The physics package of the model includes the Mellor-Yamada level 2.5 planetary boundary layer and Mellor-Yamada level 2 surface layer, large scale precipitation, convective parametrization based on the Betts, Miller and Janjić scheme, surface flux of sensible and latent heat, and radiative processes. The model physics package has been described in more detail by *Janjić* (1990, 1994).

The horizontal resolution used for the experiments was $0.25° \times 0.25°$ (28 km $\times$ 28 km) with 16 layers in the vertical. Elementary time step is 90 s. The model horizontal domain was defined between 0° to 30°E and from 40°N to 50°N.

Time-dependent lateral boundary values are taken from the ECMWF (European Centre for Medium-Range Weather Forecasts) analyses, linearly interpolated between analysed fields available at 6 h intervals. The boundary grid points of the outermost row affected by this forcing extend inwards to affect the next row. The integration domain of the model excludes these two outermost rows. The second row within the outer boundary is a blend (four-point space interpolation) of the outer row and the third row inside which is included in the integration.

4. Trajectory calculations

Trajectories can be calculated forward and backward in time. Forward trajectories are calculated within the Eta Model itself. Backward trajectories are calculated in a separate program using wind data saved from a model simulation.

The horizontal wind components (u, v) from the Eta Model are defined on a latitude-longitude (λ, φ) grid, and vertical component of motion is $\dot{\eta} = \frac{d\eta}{dt}$, defined on each eta surface of the model. For a given position and time, the new location for an integration of one trajectory time step (temporal in this study) was accomplished by a two-step approach. To derive the needed wind components at a given position, bilinear horizontal and linear vertical interpolation are performed. First, bilinear interpolation is performed horizontally on the two model η levels which are above and below the trajectory position in the vertical. Then, linear vertical interpolation is done of two horizontally interpolated values to obtain the wind component at the parcel position. This interpolation is done for all three wind components. Using these interpolated wind components (u_1, v_1, $\dot{\eta}_1$), a first guess of the new position (λ_1, φ_1, η_1) for the parcel was obtained by

$$\lambda_1^{\tau+1} = \lambda^{\tau} + u_1 \Delta t \frac{180/\pi}{R \cos \varphi^{\tau}}, \tag{1}$$

$$\varphi_1^{\tau+1} = \varphi^{\tau} + v_1 \Delta t \frac{180/\pi}{R}, \tag{2}$$

$$\eta_1^{\tau+1} = \eta^{\tau} + \dot{\eta}_1 \Delta t, \tag{3}$$

where

$$u_1 = u_1(\lambda^{\tau}, \varphi^{\tau}); \quad v_1 = v_1(\lambda^{\tau}, \varphi^{\tau}); \quad \dot{\eta}_1 = \dot{\eta}_1(\lambda^{\tau}, \varphi^{\tau}). \tag{4}$$

A new set of wind components was then calculated in the same manner for this new location, i.e.,

$$u_2 = u_2(\lambda^{\tau+1}, \varphi^{\tau+1}); \quad v_2 = v_2(\lambda^{\tau+1}, \varphi^{\tau+1}); \quad \dot{\eta}_2 = \dot{\eta}_2(\lambda^{\tau+1}, \varphi^{\tau+1}). \tag{5}$$

The final displacement was calculated using the average of the two sets of wind components:

$$\lambda_2^{\tau+1} = \lambda^{\tau} + \frac{1}{2}(u_1 + u_2)\Delta t \frac{180/\pi}{R\cos\frac{1}{2}(\varphi_1^{\tau+1} + \varphi_1^{\tau})}, \tag{6}$$

$$\varphi_2^{\tau+1} = \varphi^{\tau} + \frac{1}{2}(v_1 + v_2)\Delta t \frac{180/\pi}{R}, \tag{7}$$

$$\eta_2^{\tau+1} = \eta^{\tau} + \frac{1}{2}(\dot{\eta}_1 + \dot{\eta}_2)\Delta t. \tag{8}$$

This procedure is repeated until the desired final time is reached. Backward trajectories are calculated in the same way except for using a negative time step Δt.

5. Error statistics

In order to assess quantitatively the deviation of air parcel trajectories due to various wind data frequency, mean absolute errors (*MAE*) and mean relative errors (*MRE*) are calculated. The longitude-latitude positions of each trajectory positions were transformed to x-y positions using a map projection transformation in order to calculate the error statistics described in the following.

The *MAE* are separated into horizontal (*MAEH*) (in kilometers) and vertical (*MAEV*) (non-dimensional value of eta coordinate between 0 and 1) directions. They may be written as

$$MAEH(t) = \frac{1}{N}\sum_{n=1}^{N}\left\{\left[x_c^n(t) - x_e^n(t)\right]^2 + \left[y_c^n(t) - y_e^n(t)\right]^2\right\}^{1/2}, \tag{9}$$

$$MAEV(t) = \frac{1}{N}\sum_{n=1}^{N}\left|\eta_c^n(t) - \eta_e^n(t)\right|, \tag{10}$$

where x, y and η show the location of an air parcel, the superscripts denote the trajectory number, and the subscripts denote the control (c) or experimental (e) case. During the 48-hour integration, some trajectories move out of the model domain (especially where the transport speed is high). The *MAEH* and *MAEV* are therefore computed only with the parcels, N, available within the domain.

Although the *MAEH* and *MAEV* show the absolute transport errors, it is also important to look at the mean relative errors (*MRE*), i.e., the mean absolute errors relative to the mean total transport distance. Here, we define the

parameters, *MREH* and *MREV* as

$$MREH(t) = \frac{MAEH(t)}{THT(t)}, \tag{11}$$

$$MREV(t) = \frac{MAEV(t)}{TVT(t)}, \tag{12}$$

where *THT* and *TVT* are the mean total absolute horizontal and vertical transport distance of a control case. They are defined as

$$THT(t) = \frac{1}{N}\sum_{n=1}^{N}\left\{\left[x_c^n(t) - x_c^n(t_0)\right]^2 + \left[y_c^n(t) - y_c^n(t_0)\right]^2\right\}^{1/2}, \tag{13}$$

$$TVT(t) = \frac{1}{N}\sum_{n=1}^{N}\left|\eta_c^n(t) - \eta_c^n(t_0)\right|, \tag{14}$$

where $x_c^n(t_0)$, $y_c^n(t_0)$, $\eta_c^n(t_0)$ are the initial location of an air parcel n, and $x_c^n(t)$, $y_c^n(t)$, $\eta_c^n(t)$ are its location at time t. Use of *THT* and *TVT* definitions is limited to strong straight flow fields, such as Bora and Koshawa winds. These definitions need some modifications in the case of circular flow fields (cyclone, trough, anticyclone, etc.).

6. Forecast trajectories

From December 1, 00:00 UTC to December 3, 1990, 00:00 UTC, a typical cyclonic Bora case occurred, and a typical Koshawa case was from December 5, 00:00 UTC to December 7, 1995, 00:00 UTC. The numerical simulations were initialized at December 1, 1990, 00:00 UTC and at December 5, 1995, 00:00 UTC using ECMWF analysis. The time-dependent boundary values of the prognostic variables were updated by the linear time interpolation of the ECMWF analyses taken at 6 h intervals.

Using simulated wind, forward trajectories were calculated starting from the lowest eight model levels (LT=1 with approximate height of z=3820 m; LT=2, z=3057 m; LT=3, z=2380 m; LT=4, z=1784 m; LT=5, z=1264 m; LT=6, z=818 m; LT=7, z=442 m; and LT=8, z=136 m). Cluster analysis of trajectories in both cases were made with 5 initial points in horizontal,

central point plus 4 points with $\pm 1°$ relative to the central in both λ and φ directions. Total number of trajectories were 280 in each case.

Sensitivity to the wind data frequency is studied by varying the time step of model trajectory in the experiments, and comparing calculated trajectories with the control case, which used wind data at the highest temporal frequency available, that is, 90 s. Six experiments used the simulated wind field at smaller temporal frequencies. The first used the winds every 15 min, the second every 30 min, the third every 1 h, the fourth every 3 h, the fifth every 6 h and the sixth every 12 h.

6.1 Bora case

The control 48 h three-dimensional trajectories have been calculated forward at seven levels for the selected initial central position $\lambda=20°$, $\varphi=47°$ and are shown in *Fig. 2*. Trajectory departing from the lowest model level (LT=8 at z=136 m or $\eta=0.98$) was largely blocked by the mountains early in the integration and is not shown in the plots. Accumulation of air associated with small wind speed and moderate lifting of incoming air in front of mountains can be observed. This is evidenced by small distances between one-hour positions on the trajectories. A stronger Bora wind speed and its acceleration during descent can be seen just over and in the lee of mountains. The trajectories originating at levels 1 and 2 (LT=1 and LT=2) are outside the Bora layer. The trajectory departing from the level 7 was strongly affected by mountains so that it was rising continuously changing direction after 16 h and forming an S-like shape.

The trajectory originating from level 3 (LT=3, z=2380 m) ascends until 20 h of integration (*Fig. 2b*). Between 20 and 31 h the trajectory descends down the slope of the Dinaric Alps (*Fig. 2a*). After that, this trajectory ascends again until 33 h, then descends once more over Italian coast until 39 h. After that the air particle rises inside a low pressure system. There are two local wind speed maxima along this trajectory. One is at 31 h with speed of 19 m s^{-1} in accelerate falling over Dinaric Alps. The second one is over Italy at 35 h, with speed of 21 m s^{-1}.

The trajectory departing from level 4 (LT=4, z=1784 m) rises until 14 h of integration (Fig. 2b). It then descends until 19 h, down the slope of the Dinaric Alps (Fig. 2a). After ascending briefly it descends again, eventually leaving the model domain at 29 h. A maximum wind speed is attained at 17 h of 21 m s^{-1}. Another maximum wind speed along this trajectory occurs at 21 h over the lee sides of the Apennine Alps with the value of 26 m s^{-1}.

The trajectory originating from level 5 (LT=5, z=1264 m) ascends until 18 h and then descends until 23 h. Along this trajectory segment a maximum wind speed is achieved at 19 h of 17.5 m s^{-1}. After that the parcel rises again until 27 h over Italy, and then descends until 29 h over the lee side of the Apennine Alps, attaining a maximum wind speed of 17 m s^{-1}.

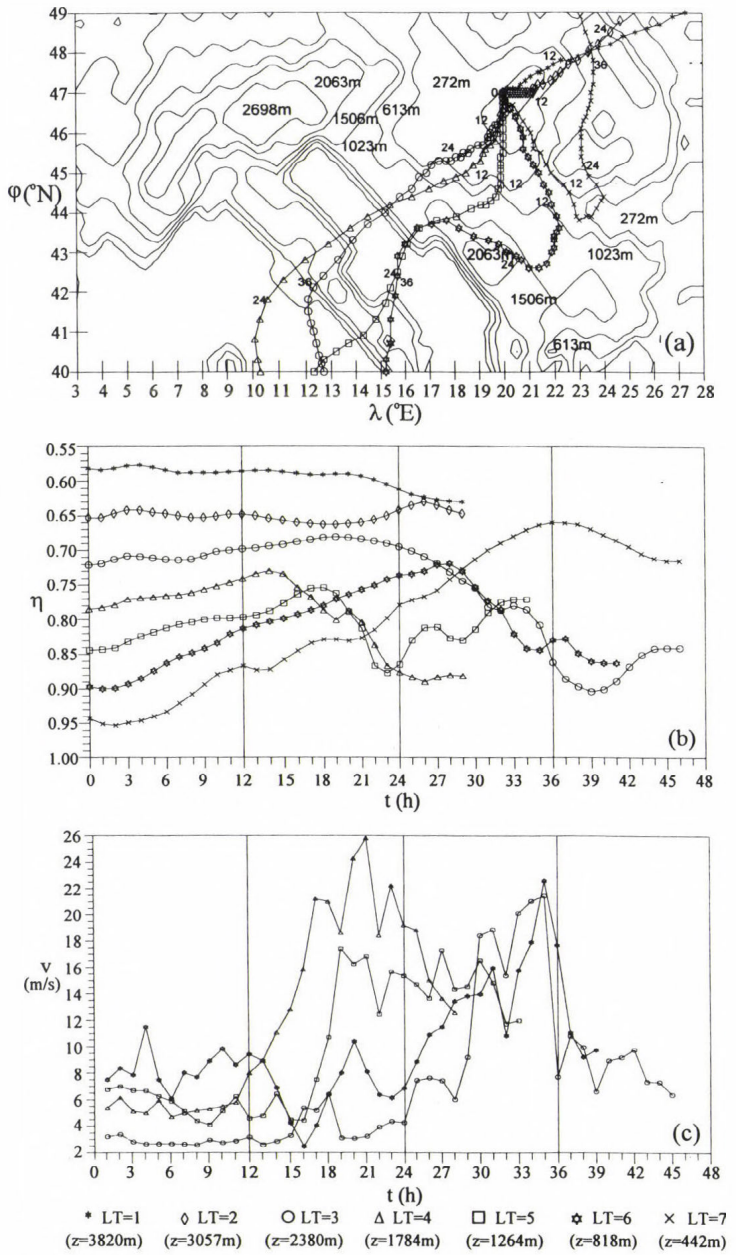

Fig. 2. Trajectories in Bora control case: (*a*) horizontal positions (numbers along trajectories indicate the time of integration in hours) and model orography; (*b*) vertical positions; (*c*) wind speed along trajectories.

The trajectory departing from level 6 (LT=6, z=818 m) ascends until 28 h. It then descends until 35 h over the lee side of the Dinaric Alps, achieving a maximum wind speed of 22 m s^{-1}. After that it rises again until 37 h, over Italy, and then descends once more. It leaves the integration domain at 41 h.

The trajectories based on the 15 min, 30 min and 1 h data are very similar to the control case, while the trajectories based on the 3 h, 6 h and 12 h data show considerable differences. Differences are larger in cases with larger time step. Increasing time step of wind data in the experiments, we notice a decrease in the maximum wind speed.

6.2 Koshawa case

The control 48 h three-dimensional trajectories have been calculated forward at seven levels for the selected initial central position $\lambda=24°$, $\varphi=44°$ and are shown in *Fig. 3*. Trajectory departing from the lowest model level (LT=8 at z=136 m or $\eta=0.98$) was blocked by the mountains (step eta orography of 272 m) in the initial position and is not shown in the plots.

In contrary to Bora case, in this case all trajectories increased speed early in the integration. A maximum speed was around at 3 h of integration, placed in the channel type of orography in Iron Gate through the Carpathians. All trajectories ascend in the beginning over orography steps of 613 m, 1023 m and some of them over 1506 m, and then descend over the lee side of the Carpathians. The low level jet is simulated at 1200 m with wind speed of 25 m s^{-1}. At the same time a maximum speed was 21 m s^{-1} at level of 800 m, and a maximum speed was 22 m s^{-1} at level of 1800 m.

The trajectories originating at levels 1 and 2 (LT=1, z=3820 m and LT=2, z=3057 m) have the near southerly direction increasing the height over the orography model step of 1506 m of the Carpathians (*Fig. 3a, b*). The trajectory originating from level 3 (LT=3, z=2380 m) has a maximum horizontal wind speed of 18 m s^{-1} at 3 h of integration, above orography step of 1506 m (*Fig. 3a, c*). The trajectory departing from level 4 (LT=4, z=1784 m) has a maximum wind speed at 3 h of 22 m s^{-1}, just over orography step of 1506 m.

The trajectory originating from level 5 (LT=5, z=1264 m) has a maximum wind speed at 3 h of 25 m s^{-1}. That is a low level jet of Koshawa wind, located at around 1200 m in vertical direction, with southeasterly direction, in the channel type of orography through the Carpathians. The trajectory departing from level 6 (LT=6, z=818 m) achieves a maximum wind speed of 21 m s^{-1} at 3 h. The trajectory originating from level 7 (LT=7, z=442 m) has a maximum wind speed at 4 h of 12 m s^{-1}. Typical distribution of wind speed along trajectories coincides with observations of Koshawa. Wind speed decreases in all trajectories after passing the Koshawa region.

The trajectories based on the 15 min, 30 min and 1 h data are very similar to the control case, while the trajectories based on the 3 h, 6 h and 12 h data

show considerable differences. Differences are larger in cases with larger time step. Increasing time step of wind data in the experiments, we notice a decrease in the maximum wind speed.

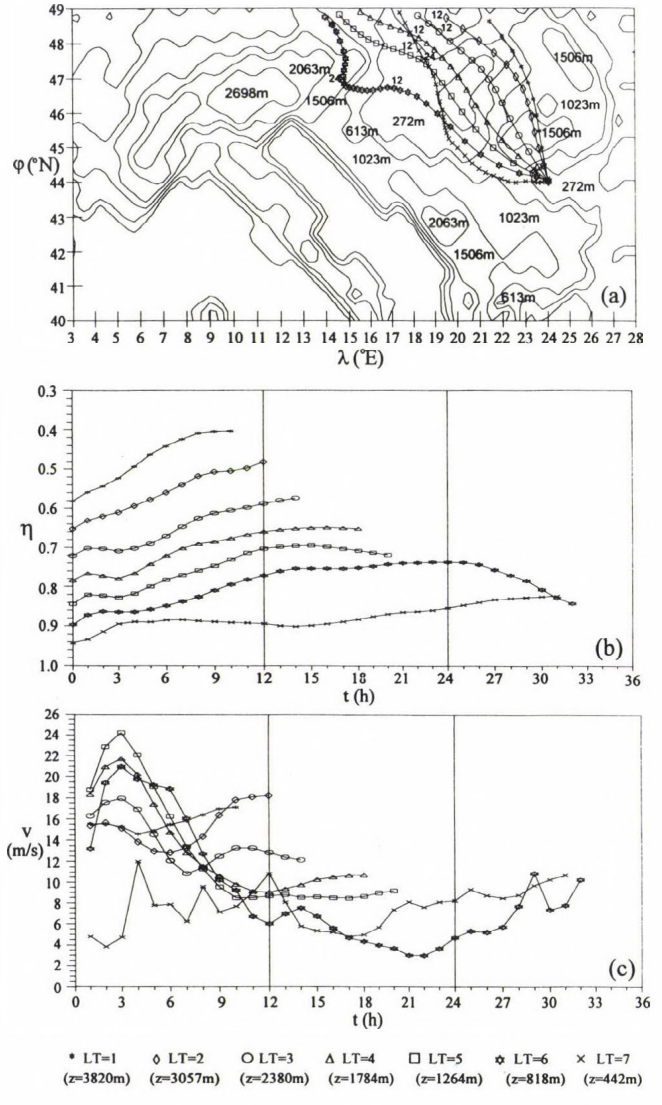

Fig. 3. Trajectories in Koshawa control case: (*a*) horizontal positions (numbers along trajectories indicate the time of integration in hours) and model orography; (*b*) vertical positions; (*c*) wind speed along trajectories.

7. Overall results

Mean absolute error in horizontal direction (*MAEH*), mean relative error in horizontal direction (*MREH*), mean absolute error in vertical direction (*MAEV*) and mean relative error in vertical direction (*MREV*) have been calculated from 280 trajectories in each data set. During the 48-hour integration, some trajectories moved out of the model domain (especially where the transport speed was high). The error statistics were computed only with the parcels, available within the domain and presented up to 36 h. Therefore in each data set in all experiments, 4515 locations were compared with the control case.

7.1 Bora case

During 24 h of integration in cases of 15 min, 30 min and 1 h wind data time step the *MAEH* remains below or at 50 km, and the *MAEH* is less than 150 km at the end of 36 h interval (*Fig. 4a*). The *MAEH* in cases of 3, 6 and 12 h wind data time steps continuously increases during the whole period, with values between 100 and 250 km at 24 h and between 250 and 400 km at 36 h of integration (Fig. 4a).

The *MREH* is less than 10% up to 24 h, and remains below 25% between 24 and 36 h of integration in cases of 15 min, 30 min and 1 h wind data time steps (*Fig. 4b*). The *MREH* in cases of 3, 6 and 12 h wind data time steps is between 15 and 80%. The *MREH* is between 40 and 60% in case of 12 h wind data time step.

The *MREH* of all trajectories is initially quite high when the absolute errors are typically comparable to or larger than the transport distance. The error stabilizes near 8% after about 3 h in cases of 15 min, 30 min and 1 h wind data time steps.

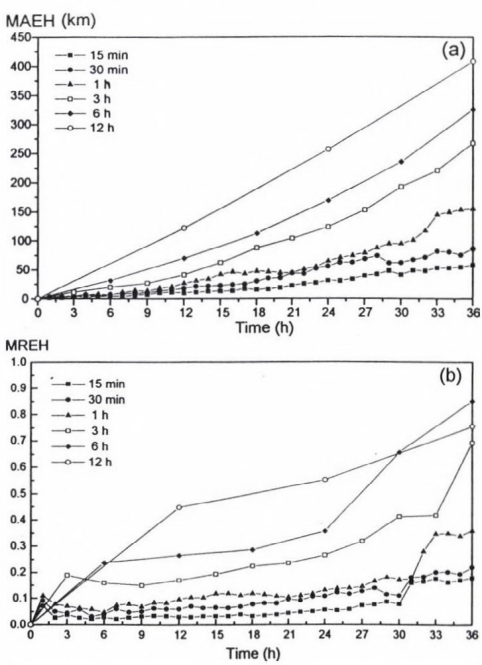

Fig. 4. The mean errors in horizontal direction in Bora case: (*a*) the mean absolute error (*MAEH*) and (*b*) the mean relative error (*MREH*).

The errors increase significantly in some cases from 30 to 33 h of integration as a result of trajectories living the domain and thus suddenly decreasing the number of trajectories available for the mean absolute error calculations.

The *MAEV* is less than 0.01 (approximately 65 m) up to 24 h, and remains under 0.04 (approximately 250 m) between 24 and 36 h of integration in cases of 15 min, 30 min and 1 h wind data time steps (*Fig. 5a*). The *MAEV* is between 0.01 and 0.05 (65–300 m) up to 24 h in cases of 3, 6 and 12 h wind data time steps. Between 24 and 36 h of integration this error varies between 0.03 and 0.14. Maximum value of the *MAEV* reaches near 0.14 at 36 h in case of 12 h wind data time step.

The *MREV* remains below 25% up to 24 h, and is less than 50% between 30 and 36 h of integration in cases of 15 min, 30 min and 1 h wind data time steps (*Fig. 5b*). The *MREV* in cases of 3, 6 and 12 h wind data time steps is between 25 and 100%. Between 24 and 36 h of integration this error varies between 50 and 200%. The *MREV* has a maximum by 36 h of about 200% in case of 12 h wind data time step.

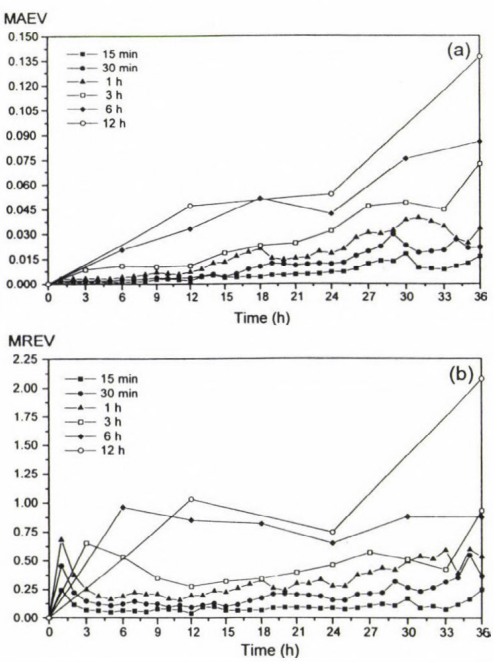

Fig. 5. The mean errors in vertical direction in Bora case: (*a*) the mean absolute error (*MAEV*) and (*b*) the mean relative error (*MREV*).

The *MREV* of all trajectories is initially quite high when the absolute errors are typically comparable to or larger than the transport distance. The error stabilizes near 20% after about 4 h in cases of 15 min, 30 min and 1 h wind data time steps.

7.2 Koshawa case

The *MAEH* increases during integration remaining below 50 km in cases of 15 min, 30 min and 1 h wind data time steps (*Fig. 6a*). Error variations in these cases are very similar to each other, with smaller values in cases with 15 and 30 min. In cases of 3, 6 and 12 h wind data time steps the *MAEH* increases during the whole period, with values between 150 and 450 km at 36 h of integration (Fig. 6a).

The *MREH* remains under 5% in cases of 15 min, 30 min and

1 h wind data time steps during the whole period of integration (*Fig. 6b*). The *MREH* is between 10 and 35% in cases of 3, 6 and 12 h wind data time steps.

The *MREH* of all trajectories is initially quite high when the absolute errors are typically comparable to or larger than the transport distance. After about 10 h the error stabilizes near 2% in cases of 15 min, 30 min and near 4% in case of 1 h wind data time step.

The *MAEV* remains below 0.01 (approximately 65 m) in cases of 15 min, 30 min and 1 h wind data time steps (*Fig. 7a*). The *MAEV* is between 0.025 and 0.105 (160–600 m) in cases of 3, 6 and 12 h wind data time steps.

The *MREV* is about 10% in cases of 15 min, 30 min and 1 h wind data time steps (*Fig. 7b*). In cases of 3, 6 and 12 h wind data time steps the *MREV* is between 40% (for 3 h time step case) and 80% (for 12 h time step case).

The *MREV* of all the trajectories is initially quite high when the absolute errors are typically comparable to or larger than the transport distance. After about 9 h the error stabilizes near 5% in cases of 15 min, 30 min and near 10% in case of 1 h wind data time step.

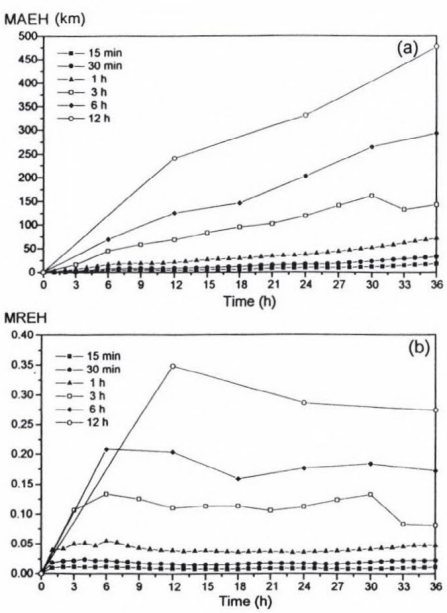

Fig. 6. The mean errors in horizontal direction in Koshawa case: (*a*) the mean absolute error (*MAEH*) and (*b*) the mean relative error (*MREH*).

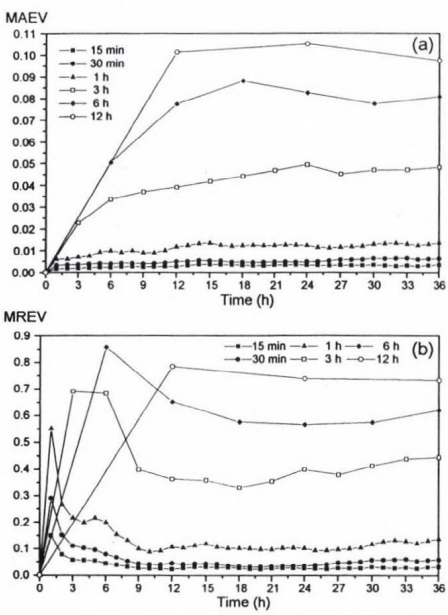

Fig. 7. The mean errors in vertical direction in Koshawa case: (*a*) the mean absolute error (*MAEV*) and (*b*) the mean relative error (*MREV*).

8. Conclusions

Numerical experiments with different frequencies of wind data in trajectory calculations of the Bora and Koshawa local winds were performed. Three-dimensional trajectories in these experiments were calculated and inspected. Forward trajectories, calculated using the Eta Model, showed changes in their behavior when comparing calculations in control case with cases of 15 min, 30 min, 1 h, 3 h, 6 h and 12 h wind data frequencies. Increasing time step of wind data in the experiments, the maximum wind speed decreased along the trajectories.

In order to assess quantitatively the deviation of air parcel trajectories due to various wind data frequencies, mean absolute error (distance between reference and forecast trajectory), mean relative error (mean absolute error divided by mean reference trajectory total transport distance) were calculated. The mean absolute error and the mean relative error were separated into horizontal and vertical directions. In each data set, calculation was done for the clusters of 280 trajectories, and 4515 locations were compared with the control case.

The mean relative error for all forecast trajectories was about 30% in Bora case and about 20% in Koshawa case. Trajectories with wind data frequency of 15 min, 30 min and 1 h were accurate enough, with mean relative error less than 10% in Bora case and less than 5% in Koshawa case. These statistics indicate that wind data frequency of 1 h, which is usually used in calculation of backward trajectories has small errors. This denotes that it is not necessary to memorize wind data in every time step of the model integration for calculating of backward trajectories.

The mean relative error of parcel positions along trajectories showed large values in case of 3 h, 6 h and 12 h wind data frequencies, especially in vertical direction. A maximum of the mean relative error (about 200%) was associated with forecast trajectories in vertical direction in case of 12 h wind data of Bora wind. This result suggests that trajectories calculated from the analysed wind data (12 h data frequency) are not accurate when they are used. This means that the current synoptic observational frequency is inadequate for accurate calculations of long-range transport or episodic events. This result also indicates the importance of using the vertical velocity for calculating the trajectories.

In general, Koshawa case was less sensitive to the temporal frequency of wind data than Bora case. Trajectories in Koshawa case were more precise than in Bora case because Koshawa wind is a low level jet-effect wind and more channelized by the orography at larger scales than Bora wind. The low level jet-effect wind is increased in speed through the channeling of air by some orographic configuration.

Construction of accurate three-dimensional atmospheric trajectories provides a valuable diagnostic tool for illustrating and understudying the three-dimensional flow fields and associated transports, as well as the dispersal of upper

atmospheric pollutants and possible nuclear contamination. Koshawa wind is sometimes dusty or contains air pollutants (*Vukmirović et al.*, 2000), so this investigation is also important for accurate long-range air pollution transports and environmental studies.

Acknowledgments—This study was partly supported by the Serbian Academy of Science and Art under Grant F-147 and partly by the Association for Science of Serbia under Grant 0704.

References

Chen, W.D. and *Smith, R.B.*, 1987: Blocking and deflection of airflow by the Alps. *Mon. Wea. Rev. 115*, 2578-2597.

Doty, K.G. and *Perkey, D.J.*, 1993: Sensitivity of trajectory calculations to the temporal frequency of wind data. *Mon. Wea. Rev. 121*, 387-401.

Haagenston, P.L., Gao, K. and *Kuo, Y.H.*, 1990: Evaluation of meteorological analyses, simulations, and long-range transport calculations using ANATEX surface tracer data. *J. Appl. Meteor. 29*, 1268-1283.

Heffter, J.L., Stunder, B.J.B. and *Rolph, G.D.*, 1990: Long-range forecast trajectories of volcanic ash from Redoubt volcano eruption. *Bull. Amer. Meteor. Soc. 71*, 1731-1738.

Janjić, Z.I., 1990: Physical package for the step-mountain, eta coordinate model. *Mon. Wea. Rev. 118*, 1429-1443.

Janjić, Z.I., 1994: The step-mountain eta coordinate model: Further developments of the convection, viscous sublayer and turbulence closure schemes. *Mon. Wea. Rev. 122*, 927-945.

Küttner, J., 1940: Der Koshawa in Serbien. *Meteor. Z. 57*, 120-123.

Lazić, L. and *Tošić, I.*, 1998: A real data simulation of the Adriatic Bora and the impact of mountain height on Bora trajectories. *Meteorol. Atmos. Phys. 66*, No. 3-4, 143-155.

Maryon, R.H. and *Buckland, A.T.*, 1995: Tropospheric dispersion: the first ten days after a puff release. *Quart. J. Roy. Meteorol. Soc. 121*, 1799-1833.

McQueen, J.T. and *Draxler, R.R.*, 1994: Evaluation of model back trajectories of the Kuwait oil fires smoke plume using digital satellite data. *Atmos. Environ. 28*, 2159-2174.

Mešinger, F., 1984: A blocking technique for the representation of mountains in atmospheric model. *Riv. Met. Aeronautica 44*, 195-202.

Mesinger, F., Janjić, Z.I., Ničković, S., Gavrilov, D. and *Deaven, D.G.*, 1988: The step-mountain coordinate: model description and performance for cases of Alpine lee cyclogenesis and for a case of an Appalachian redevelopment. *Mon. Wea. Rev. 116*, 1493-1518.

Petersen, R.A. and *Uccellini, L.W.*, 1979: The computation of isentropic atmospheric trajectories using a Discrete Model formulation. *Mon. Wea. Rev. 107*, 566-574.

Rolph, G.D. and *Draxler, R.R.*, 1990: Sensitivity of three-dimenzional trajectories to the spatial and temporal densities of the wind field. *J. Appl. Meteor. 29*, 1044-1054.

Unkašević, M., Mališić, I. and *Tošić, I.*, 1999: Some aspects of the wind "Koshava" in the lower troposphere over Belgrade. *Meteorol. Appl. 6*, 69–80.

Vukmirović, Z., Unkašević, M., Lazić, L., Tošić, I., Rajšić, S. and *Tasić, M.*, 2000: Analysis of an exceptional Saharan dust event in Serbia using the Eta Model. Submitted to *Atmos. Res.*

Yoshino, M., 1976: *Local wind Bora*. University of Tokyo Press, Tokyo. 289 pp.

IDŐJÁRÁS

Quarterly Journal of the Hungarian Meteorological Service
Vol. 104, No. 2, April–June 2000, pp. 109–122

Numerical study of heat and moisture exchange in the morning boundary layer

Rumjana Mitzeva and **Gergana Gerova**

Department of Meteorology, Faculty of Physics, University of Sofia
5, J. Bourchier, Sofia–1126, Bulgaria
E-mail: rumypm@phys.uni-sofia.bg

(Manuscript submitted for publication 3 November 1999; in final form 25 February 2000)

Abstract—One-dimensional numerical model of the evolution of the morning convective boundary layer (CBL) for strong insolation, light wind and absence of clouds being previously developed is here completed with a study of moisture transport. The basic assumption is that heat and moisture transport in the CBL is due to discrete convective elements, i.e., thermals. Governing equations for the vertical profile of horizontal-mean virtual potential temperature and specific humidity are derived partitioning the CBL each level and each moment into two domains, one covered by thermals and another occupied by downdrafts.

The impact of the magnitude of radiation heating and moisture as well as the impact of the distribution of thermals at the earth surface on the CBL characteristics are studied and discussed. The results from the calculations with simulated and observed initial temperature and humidity profiles show that the model reasonably well simulates the heat and humidity exchange in the morning boundary layer in fair weather conditions.

Key-words: convective boundary layer, thermals, numerical model.

1. Introduction

Atmospheric movements in the convective boundary layer are of a great interest for science because of their essential impact upon nature, people and economy. There are a variety of models describing the evolution of the mixing layer (ML) which differ in their main assumptions or in the approach to the "closure" problem. The choice of a model depends on the aim of investigation and on the authors' conception.

The model developed and tested in this paper is fitted to clear-sky days with light mean winds when the dominant mechanism driving the turbulence is buoyancy, and the mechanically generated mixing by shear can be neglected.

It is based on the well-known fact that during daytime when the sun heats the ground, the air near the ground warms and rises as convective thermals. Plenty of numerical models incorporate that idea (*Telford,* 1966; *Manton*, 1975; *Andreev* and *Ganev,* 1981; *Cushman-Roisin,* 1982; *Chatfield* and *Brost,* 1987).

The model in this paper is an extension of the model presented in *Mitzeva et al.* (1997) and in addition includes the study of moisture transport.

In Section 2 one can find the model description. The numerical scheme, initial and boundary conditions are given in Section 3. The results of the numerical simulations and comparison with observations are presented in Section 4. The summary and discussion are given in the final section of the paper.

2. Model description

The main assumptions and governing equations for the calculation of virtual potential temperature (VPT) and specific humidity (SH) in the convective boundary layer (CBL) are given in this section. The argumentation of this parameterization and more details can be found in *Mitzeva et al.* (1997).

The basic idea in the model is that heat and moisture in the CBL are transported by discrete convective elements, i.e., thermals and compensating downdrafts. For the parameterization of the CBL in *Mitzeva et al.* (1997), a horizontal area of CBL, $S(z,t)$, at a given level z and given moment t is partitioned into two domains: one part of the area is covered with rising thermals (updrafts), $S_T(z,t)$, and the rest of the area is occupied by compensating downdrafts, $S_E(z,t)$, (*Fig. 1*). Thus, the vertical velocity field is used as indicator for thermals in this particular parameterization. This separation is also valid for the other CBL characteristics, because the velocity controls their spatial and temporal distribution. Following the same procedure of averaging over a horizontal area as in *Mitzeva et al.* (1997), the final set of the equations for the horizontal mean VPT, $\overline{\theta_V}$ and SH, $\overline{q}$ evolution is as follows:

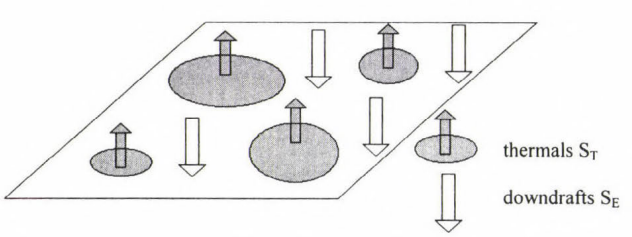

Fig. 1. Schematic illustration of the partition of CBL at a given level and given time into thermal and downdraft domains.

$$\frac{\partial \overline{\theta_V}}{\partial t} + \frac{\partial}{\partial z}\left[B(z,t)\overline{\theta_V}\right] = C(z,t), \tag{1}$$

$$\frac{\partial \overline{q}}{\partial t} + \frac{\partial}{\partial z}\left[B(z,t)\overline{q}\right] = D(z,t), \tag{2}$$

where $B(z,t)$, $C(z,t)$ and $D(z,t)$ are given by:

$$B(z,t) = \frac{1}{1 - S_T/S}\overline{W_T}, \tag{3}$$

$$C(z,t) = -\frac{\partial}{\partial z}\left[\frac{1}{1 - S_T/S}\overline{W_T}\,\overline{\theta_{VT}} + \overline{W_T}\,\overline{\theta_{VT}}\right], \tag{4}$$

$$D(z,t) = -\frac{\partial}{\partial z}\left[\frac{1}{1 - S_T/S}\overline{W_T}\,\overline{q_T} + \overline{W_T}\,\overline{q_T}\right], \tag{5}$$

and

$$\overline{W_T} = \sum_R \pi R^2 W_T(R,z,t) f(R,z,t),$$

$$\overline{\theta_{VT}} = \sum_R \pi R^2 \theta_{VT}(R,z,t) f(R,z,t),$$

$$\overline{q_T} = \sum_R \pi R^2 q_T(R,z,t) f(R,z,t),$$

$$\overline{W_T q_T} = \sum_R \pi R^2 W_T(R,z,t)\, q_T(R,z,t) f(R,z,t).$$

Here $f(R,z,t)$, $W_T(R,z,t)$, $\theta_{VT}(R,z,t)$ and $q_T(R,z,t)$ are size distribution function, vertical velocity, VPT and SH for thermal with radii R at level z and moment t, respectively. The individual thermals' characteristics (W_T, θ_{VT}, q_T) are

obtained from Eqs. (6) to (8). The sum $\sum_R$ is over all thermals' radii. The fraction of the area occupied by rising thermals at level z and moment t is calculated by:

$$S_T/S = \sum_R \pi R^2 f(R,z,t).$$

The downdraft characteristics are presented by the mean values dependent on time and height based on the observations showing that the downdraft velocity distribution is rather narrow and has a mode approximately equal to the average downdraft velocity (*Lamb*, 1982).

The thermals are considered as discrete convective elements with various sizes originating near the surface after sunrise (a.s.r.) and lifting in upward direction without interactions with each other, i.e., vertical and horizontal mixing between different thermals are not included in the model. Similar to *Andreev* and *Ganev* (1981) it is assumed that the thermals are spheres with radii R and their characteristics are calculated according to *Andreev* and *Panchev* (1975):

$$\frac{dW_T(R,z,t)}{dt} = -\alpha W_T^2(R,z,t) + g\left[\frac{\theta_{VT}(R,z,t) - \overline{\theta_V}}{\overline{\theta_V}}\right], \tag{6}$$

$$\frac{d\theta_{VT}(R,z,t)}{dt} = -\alpha\left[\theta_{VT}(R,z,t) - \overline{\theta_V}\right] W_T(R,z,t), \tag{7}$$

$$\frac{dq_T(R,z,t)}{dt} = -\alpha\left[q_T(R,z,t) - \overline{q}\right] W_T(R,z,t) \tag{8}$$

and

$$\frac{dz}{dt} = W_T,$$

where g is acceleration of gravity and α is entrainment parameter. In this study the simple parametrization for α (see *Andreev* and *Panchev*, 1975) was used, based on the assumption for the inverse relationship between entrainment rate and thermal radius, i.e., $\alpha=0.6/R$.

The calculations of terms $B(z,t)$, $C(z,t)$ and $D(z,t)$ require information about the size distribution function $f(R,z,t)$ at any level and moment. In order to determine $f(R,z,t)$, the thermals are transformed into cylinders with the same radius R and volume as the spherical ones, and with heights $H=4/3R$. In this manner the spherical thermals are modified to columns of rising air, that is

close to the observations showing that the idealized thermal shape is like that of a sausage (*Stull*, 1988).

It is useful to be mentioned that Eq. (1) in this paper is the same as Eq. (11) in *Mitzeva et al.* (1997), however the potential temperature is replaced here by the virtual potential temperature. Eq. (2) and Eq. (8) are added giving opportunity to study the moisture transport in the CBL.

3. Numerical scheme, initial and boundary conditions

Eqs. (1) and (2) are solved numerically by the Lax scheme (*Roache*,1976) with time step $\Delta t = 1$ s and grid length $\Delta z = 10$ m. The scheme has second-order time and space accuracy and is recommended to be used for preliminary model tests.

For numerical integration of Eqs. (6) to (8) the Runge-Kutta method is run with time step $\Delta t = 1$ s.

The initial level in the model, $z=0$, is set to be the level of the thermals starting. Although this level is in the upper boundary of the surface layer, for simplicity, we assume that $z=0$ coincides with the earth surface.

For numerical simulations the time evolution of VPT, $\overline{\theta_V}(0,t)$ and SH, $\bar{q}(0,t)$ at the initial level has to be given. The temperature at the earth surface follows the changes of the solar radiation. The lower boundary condition for the temperature is:

$$\overline{\theta_V}(0,t) = \overline{\theta_V}(0,0) + k \sin(2\pi t/24)\,(1 + 0.611\,\bar{q}(0,t)), \tag{9}$$

where $\overline{\theta_V}(0,0)$ is the VPT at the earth surface at the moment of sunrise, and k gives the increase of the earth's surface temperature for six hours. The time variations of $\overline{\theta_V}(0,t)$ for different values of the parameter k, following Eq. (9) are shown in *Fig. 2a*.

The evolution of SH near the ground $\bar{q}(0,t)$, typical for the continental area is shown by a bold line in *Fig. 2b* (*Hrgian*, 1969). It is seen that the SH increases during the first two hours and decreases in the next four hours. This evolution at the bottom boundary can be given by:

$$\bar{q}(0,t) = \bar{q}(0,0) + m \sin(2\pi t/d) \qquad \left\{\begin{array}{ll} d = 8 \text{ hours} & 0 < t \le 2 \text{ hours} \\ d = 12 \text{ hours} & 0 < t \le 6 \text{ hours} \end{array}\right\}, \tag{10}$$

where $\bar{q}(0,0)$ is the SH at the earth surface in the moment of sunrise. For the case presented by a bold line in Fig. 2b, $m = 1.6$ g kg^{-1}.

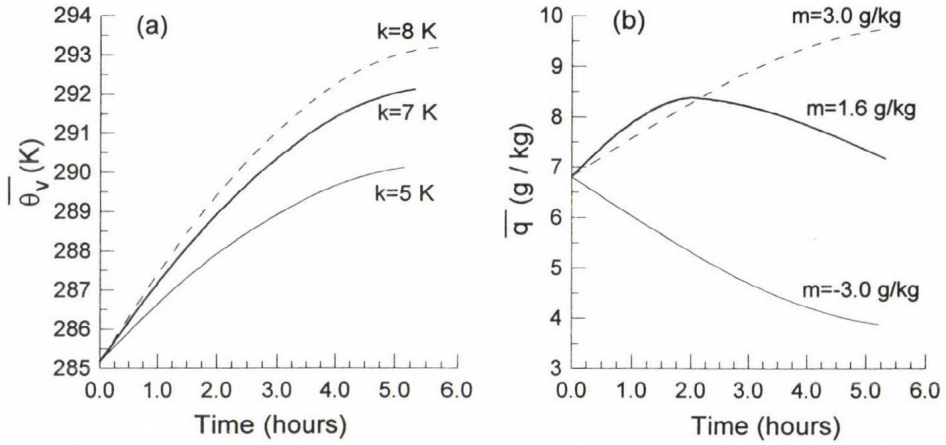

Fig. 2a. Time variations of virtual potential temperature $\overline{\theta_v}$ at the earth surface for different magnitudes of the solar heating: $k=5$ K (thin line), $k=7$ K (bold line) and $k=8$ K (dashed line).

Fig. 2b. Time variations of specific humidity $\overline{q}$ at the earth surface. The typical evolution for the continental area ($m=1.6$ g kg^{-1}) is plotted by bold line, $m=-3.0$ g kg^{-1} by thin line and $m=3.0$ g kg^{-1} by dashed line.

The model requires an initial sounding: thermal size distribution, vertical velocities, temperature and moisture excess of thermals at the earth surface to be set in. For all model calculations the starting velocities of the rising thermals are fixed to be 1 m s^{-1} and the temperature excess is set to be 1 K based on the measurements of *Telford* (1966). The calculations are carried out with $q_T(R,0,t) = \overline{q}(0,t)$, which means that the thermals at the earth surface are warmer but not moister than the environment, which is typical over the continents.

To investigate the impact of the initial thermal size distribution on heat and moisture transport, similar to *Mitzeva et al.* (1997), two types of size distribution (the number of thermals with a given diameter per km^2 at the earth's surface) were used. The first type is presented in *Table 1* and will be refer as ST1. It is extracted by *Andreev* and *Ganev* (1981) from *Vulfson*'s (1961) data. According to ST1, 22% of the earth surface area is covered with thermals for the first three hours a.s.r. and 42% for the second three hours a.s.r. This is in agreement with the results from aircraft measurements showing that updrafts cover 15–43% of the horizontal area (*Stull,* 1988). The second distribution function (ST2) presented in *Table 2* differs from ST1 in thermal

diameters, while the fraction of area occupied by thermals at the earth surface is the same as for ST1. ST2 type distribution is uniform and it is taken in some extend arbitrary in the range of thermal sizes quoted in *Warner* and *Telford* (1967).

Table 1. Size distribution of the thermals (ST1) at the earth surface. The statistics is extracted from *Vulfson's* (1961) data by *Andreev* and *Ganev* (1981)

Diameter of the thermals (m)	Number of the thermals per km^2	
	Hours after sunrise 0-3	Hours after sunrise 3-6
5	0.6	1.4
15	4.5	11.2
25	4.9	14.0
35	6.2	14.8
45	6.4	15.5
55	6.2	15.5
65	6.1	14.8
75	4.9	13.5
85	5.7	12.1
95	5.1	10.1
105	4.5	7.7
128	2.3	1.7

Table 2. Size distribution of the thermals (ST2) at the earth surface

Diameter of the thermals (m)	Number of the thermals per km^2	
	Hours after sunrise 0-3	Hours after sunrise 3-6
50	2.2	4.0
100	2.2	4.0
150	2.2	4.0
200	2.2	4.0
250	2.2	4.0

The initial VPT, $\overline{\theta_V}(z,0)$ and SH, $\overline{q}(z,0)$ profiles are linearly interpolated in order to determine the vertical grid values of VPT and SH.

The evolution of VPT and SH profiles for a time step $t+\Delta t$ are obtained following the next sub-steps:

- The Eqs. (6) to (8) are numerically integrated by the Runge-Kutta method using $\overline{\theta_V}(z,t)$ and $\overline{q}(z,t)$. Thus $W_T(R,t+\Delta t)$, $\theta_{VT}(R,t+\Delta t)$, $q_T(R,t+\Delta t)$ and $z(R,t+\Delta t)$ are calculated for the moment $t+\Delta t$.
- The discrete size distribution function $f(R,z,t)$ is determined as the sum of the thermals with radii R which at a given moment t affect the levels z situated between $z-H/2$ (bottom of the cylindrical thermal) and $z+H/2$ (top of the cylindrical thermal).
- The terms $B(z,t)$, $C(z,t)$ and $D(z,t)$ are calculated from Eqs. (3) to (5).
- $\overline{\theta_V}(z,t+\Delta t)$ and $\overline{q}(z,t+\Delta t)$ are obtained from Eqs. (1) and (2) by the Lax scheme.
- For the levels not affected by rising thermals at a given moment t, $f(R,z,t)=0$, $\overline{\theta_V}(z,t+\Delta t)=\overline{\theta_V}(z,t)$ and $\overline{q}(z,t+\Delta t)=\overline{q}(z,t)$.

These calculations are repeated until all the thermals reach the levels at which their velocity $W_T(R,z,t)=0$, i.e., at these levels the thermals lose their individuality and no longer differ from the environmental air.

In the model it is accepted that a new thermal group with a given distribution function starts at initial level when all previous thermals have stopped, but not more frequently than in every 15 minutes.

4. Numerical simulations and results

The aim of the paper is to study the possibilities of the model to simulate the vertical transport of heat and moisture after sunrise in the absence of clouds and wind. The impact of the parameters used in the model on the formation and development of the CBL is also tested.

In all numerical tests the initial temperature profile (bold line in *Figs. 3a, 4a, 5a, 6a*) corresponds to ground inversion with temperature lapse rate $\partial T/\partial z=$ 0.1 K/100 m for the layers between 0 and 600 m, and $\partial T/\partial z=-$ 0.5 K/100 m above 600 m. The initial profile of SH (bold line in *Figs. 3b, 4b, 5b, 6b*) is typical for the morning hours at sunrise.

The evolution of the horizontal-mean VPT and SH profiles during the first five hours a.s.r. are given in Fig. 3a and Fig. 3b, respectively. The calculations are carried out with $k=7$ K (bold line in Fig. 2a). The earth surface SH changes are plotted by a bold line in Fig. 2b; they correspond to an increase of SH during the first two hours (a.s.r.) followed by a decrease in the second three hours.

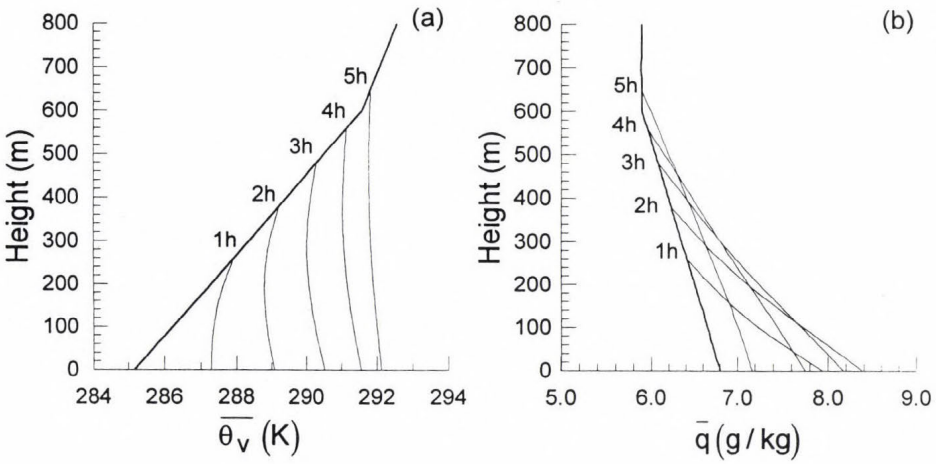

Fig. 3. Hourly vertical profiles (*a*) of the horizontal mean virtual potential temperature $\overline{\theta_v}$ (thin lines); (*b*) of the specific humidity $\bar{q}$ (thin lines). The numbers indicate the hours after sunrise. The initial profile is plotted by bold line. The magnitude of radiation heating corresponds to $k = 7$ K. The case $m = 1.6$ g kg^{-1} for the earth's surface $\bar{q}$ is used.

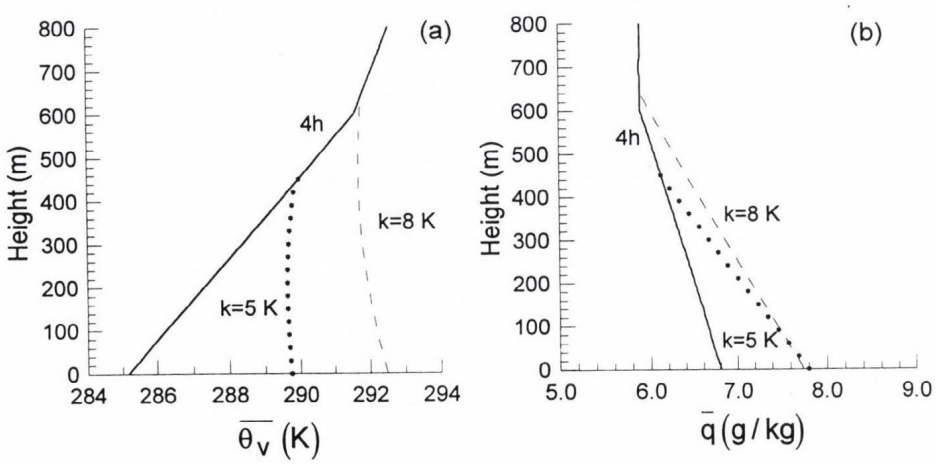

Fig. 4. Vertical profiles (*a*) of the virtual potential temperature $\overline{\theta_v}$; (*b*) of the specific humidity $\bar{q}$ for different magnitudes of radiation heating $k = 5$ K (stars) and $k = 8$ K (dashed line) four hours after sunrise. The initial $\overline{\theta_v}$ and $\bar{q}$ profiles are plotted by bold line.

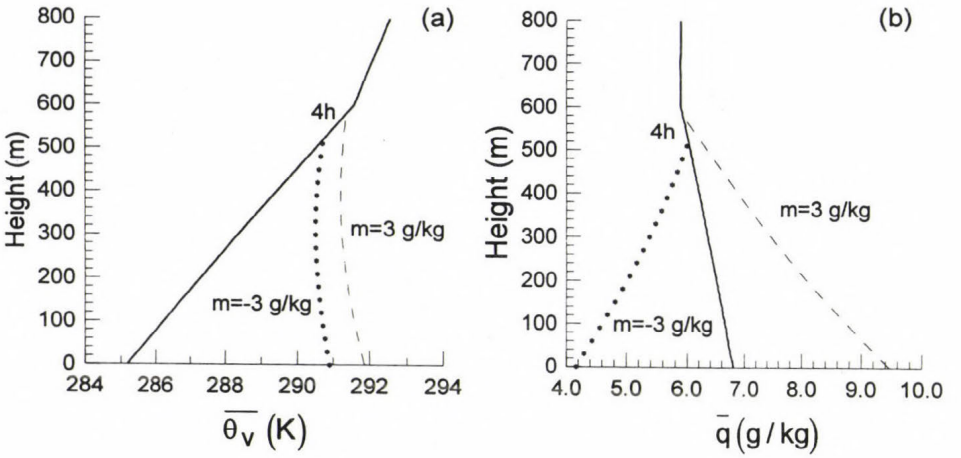

Fig. 5. Vertical profiles (*a*) of virtual potential temperature $\overline{\theta_v}$; (*b*) of specific humidity $\bar{q}$ four hours after sunrise for different values of the earth's surface specific humidity: $m=-3.0$ g kg^{-1} (stars) and $m=3.0$ g kg^{-1} (dashed line). The initial $\overline{\theta_v}$ and $\bar{q}$ profiles are plotted by bold line.

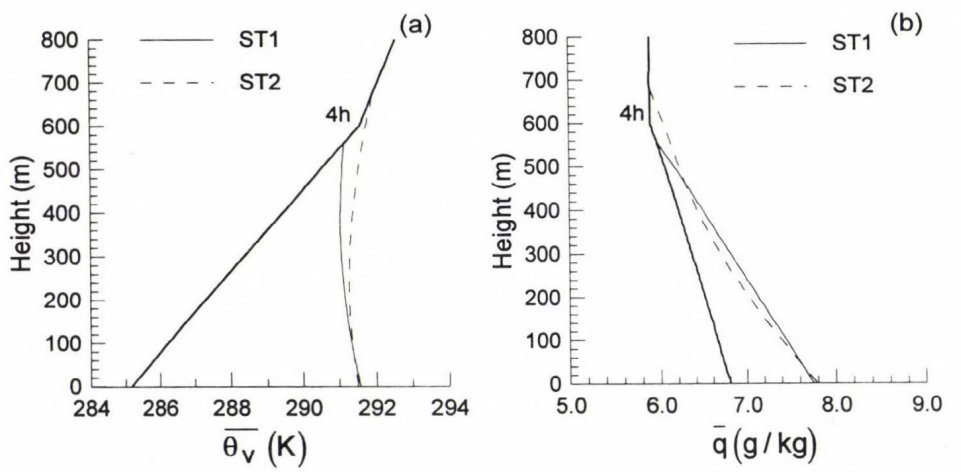

Fig. 6. Vertical profiles (*a*) of virtual potential temperature $\overline{\theta_v}$; (*b*) of specific humidity $\bar{q}$ four hours after sunrise: thin line — ST1 distribution, dashed line — ST2 distribution. The initial $\overline{\theta_v}$ and $\bar{q}$ profiles are given by bold line.

Fig. 3a shows that according to the model calculations, CBL depth grows with time and five hours a.s.r. the CBL height is approximately 650 m. It is seen also that VPT has a minimum near the middle of the CBL, because heating from below (by rising thermals) and entrainment of warm air from above (by downdrafts) lead to slightly warmer VPT in those regions. This result is in agreement with the mean VPT profile in the CBL (*Stull*, 1988). The moisture, presented in Fig. 3b, is redistributed to the same level as VPT. In this particular case the moisture at the earth surface is always greater than the moisture on the upper levels, i.e., a negative gradient in the ML is obtained. This result can be related to the fact that the updrafts transport moist air from the earth surface, while the downdrafts bring drier air from above. Based on the above, one can conclude that the model simulates the evolution of VPT and SH profiles in the morning boundary layer in agreement with generally accepted assumptions for the phenomena under study (*Stull,* 1994).

To study the model reaction to the rate of surface heating, the calculations are carried out with $k=5$ K and $k=8$ K. Fig. 4a shows that the magnitude of solar heating influences strongly the depth of CBL—the greater the heating, the higher the mixed layer is. Four hours a.s.r. the ML developed up to 450 m in the case of $k=5$ K (stars) and up to 640 m at $k=8$ K (dashed line). Fig. 4b shows that SH close to the ground is bigger at a greater solar heating. The comparison of SH at level $z=400$ m gives $q=6.3$ g kg^{-1} in the case of $k=5$ K and $q=6.6$ g kg^{-1} in the case of $k=8$ K, i.e., the difference is about 0.3 g kg^{-1}. This is due to the fact that greater number of thermals have reached height $z=400$ m when the heating is stronger.

The impact of the SH changes at the earth surface on the CBL depth is tested using two different values of the parameter m in Eq. (10) ($d=12$ hours for $0<t<6$ hours). Model outputs with $k=7$ K are shown in Fig. 5a (VPT profile) and Fig. 5b (SH profiles). Results corresponding to an increase of the earth surface SH ($m=3$ g kg^{-1}) are given by dashed lines; stars show the results with $m=-3$ g kg^{-1}, i.e., a decrease of the earth surface SH. It is clear from Fig. 5a that a significant increase in SH at the earth surface leads to slight increase in the CBL height. Four hours a.s.r. the difference in the CBL height is less than 60 m for 4.3 g kg^{-1} difference in the earth surface SH. The changes of SH at the earth surface however are of great importance for the moist quantity reaching the upper levels. The greater the SH at the earth surface, the greater the moisture in the ML is—four hours a.s.r. the SH at 300 m is 7.5 g kg^{-1} in the case of $m=3.0$ g kg^{-1} and 5.4 g kg^{-1} in the case of $m=-3.0$ g kg^{-1}. In comparison with the ground SH, the moisture decreases with height in the case of $m=3.0$ g kg^{-1}, due to the transport of drier air by downdrafts. An increase of the SH with height is observed at $m=-3.0$ g kg^{-1} explained with the fact that downdrafts contain more humid air than updrafts. In conclusion it can be said that the ground moisture influences significantly the SH profile, and its effect on the VPT redistribution and the ML depth is not well pronounced.

The sensitivity of the model to the size distribution of thermals at the earth is visible from Figs. 6a and 6b, where the calculated VPT and SH profiles by two types of size distribution ST1 (thin line) and ST2 (dashed line) are presented four hours a.s.r. The results show that when heat and moisture are transported by larger thermals (ST2 type distribution), the changes in VPT and SH profiles extend for approximately 100 m higher than the corresponding extend for changes caused by smaller thermals (ST1 type distribution). Although the thermals occupied one and the same fraction of area at the earth surface, the larger thermals (ST2) can ascend higher than smaller ones, (ST1), due to the smaller entrainment of the environmental air, hence the higher levels are affected.

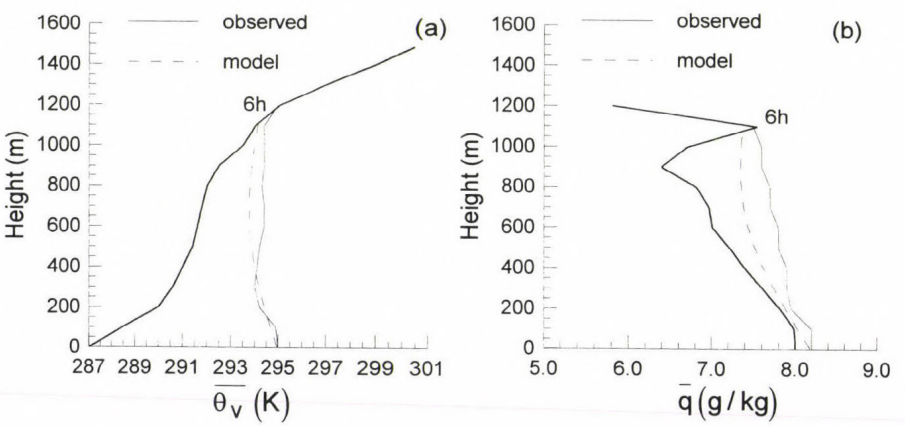

Fig. 7. Vertical profiles (*a*) of virtual potential temperature $\overline{\theta_v}$; (*b*) of specific humidity $\bar{q}$ six hours after sunrise: thin line – observation data, dashed line – model output. The initial profiles of measured $\overline{\theta_v}$ and $\bar{q}$ is given by bold line.

To check the capacity of the presented model to reproduce the evolution of the ML characteristics, the early morning sounding (05:21 LST on July 8, 1986) of the field experiment HAPEX-MOBILHY is chosen. This day is reported as a purely convective case. The initial VPT and SH profiles are taken from Figs. 1a and 2a in *Cuxart et al.* (1994) and plotted by bold lines in *Fig. 7a* and *Fig. 7b*, respectively. The values for k and m for the calculations of $\overline{\theta_v}(0,t)$ and $\bar{q}(0,t)$ are chosen to fit the observed evolution of VPT and SH at the earth surface. Due to the lack of information about size distribution of thermals at the earth surface, the model was run by ST1 and ST2. The results

shows that six hours a.s.r. the calculated by ST1 height of CBL is about 950 m, which is 200 m lower than the measured one. Using ST2 distribution function, six hours a.s.r. the modeled ML depth is close to the observed value at 11:14 LST. On account of this, model results using ST2 thermal size distribution six hours a.s.r. (dashed lines on Fig. 7a and Fig. 7b) are compared with corresponding observations (thin lines on Fig. 7a and Fig. 7b). The comparison shows that the model does not reproduce perfectly well the VPT values. However the difference between modeled and observed VPT is less than 0.6°C. The observed VPT profile supports the small stable gradient predicted by the model. Six hours a.s.r. the predicted SH profile in the CBL (dashed line in Fig. 7b) is also quite similar to the observed one (thin line in Fig. 7b), but the calculated vertical gradient is greater than the observed one. The difference between modeled and measured SH is the greatest at $z=500$ m and it is about 0.4 g kg^{-1} there. It is worthwhile to mention that the observed case is an interesting example for moisture redistribution—the moisture in the ML is transported by the moist updrafts and downdrafts. To summarize the results from comparison between model calculations and field measurements it can be said that the main features of VPT and SH profiles are well simulated.

5. Summary and conclusion

A one-dimensional numerical model of the evolution of the morning convective boundary layer is developed. The basic idea of the model is that the heat and moisture in the convective mixed layer are transported by isolated turbulent eddies (thermals). The model is applicable to the clear-sky days with light mean winds when the dominant mechanism driving the turbulence is the buoyancy. The partition of the CBL into updrafts and compensating downdrafts domains as in *Mitzeva et al.* (1997) leads to the equations for the evolution of horizontal-mean virtual potential temperature and specific humidity. The problem is closed by assuming that thermals ascend as individual ones entraining the environmental air. For the numerical study of the vertical profiles of the horizontal-mean VPT and SH, the vertical velocities, the temperature excesses and size distribution function of thermals at the earth surface are preassigned in accordance to the observations.

The results of the calculations with simulated and observed initial temperature and humidity profiles show that the model reproduces satisfactory well the main features of VPT and SH evolution in the CBL. The model output for VPT shows a slightly unstable lapse rate in the lower part of the CBL and a slightly stable lapse rate in the upper part of the CBL, which is consistent with the observations. The negative gradient in SH is obtained by the model at variations of the earth's surface SH typical for the morning hours. This result is in agreement with the field measurements.

The numerical test indicates the importance of the magnitude of solar heating for the depth of CBL—the greater the heating, the higher the developed mixed layer is. The simulations with the model show that the earth surface SH influences significantly the moisture gradient in the ML and its effect on the CBL height and on the VPT profile is less significant than the magnitude of solar heating.

The numerical experiments and the comparison between model simulations and observations reveal the sensitivity of the model to the distribution of thermals at the starting level, which implies that the determination of these quantities from field measurements would be useful for this type of model.

The parametrization of the thermals' merger during their ascend and the sink of thermals back into the ML after penetrating the temperature inversion will bring the model closer to the physical nature of the phenomenon.

Acknowledgements—This work is partly supported by the Bulgarian Science Foundation grand NZ-610/96. We would like to thank *Dr. K. Ganev* for the useful comments concerning the numerical scheme and *Dr. St. Evtimov* for remarks and discussions.

References

Andreev, V. and *Panchev, S.*, 1975: *Dynamics of Atmospheric Termals* (in Russian). Gidrometeoizdat, Leningrad.

Andreev, V. and *Ganev, K.*, 1981: Model of convective heat exchange due to isolated thermals in the atmospheric boundary layer. *Boundary-Layer Meteorol. 20*, 331-339.

Chatfield, R.B. and *Brost, R.A.*, 1987: A two-stream model of the vertical transport of trace species in the convective boundary layer. *J. Geophys. Res. 92*, 13263-13276.

Cushman-Roisin, B., 1982: A theory of convection. Modeling by two buoyant interacting fluids. *Geophys. Astrophys. Fluid Dynamics 19*, 35-59.

Cuxart, J., Bougeault, P., Lacarrere, P., Noilhan, J. and *Soler, M.R.*, 1994: A comparison between transilient turbulence theory and the exchange coefficient model approaches. *Boundary-Layer Meteorol. 67*, 251-276.

Hrgian, A.X., 1969: *Physics of the Atmosphere* (in Russian). Gidrometeoizdat, Leningrad.

Lamb, R.G., 1982: Diffusion in the convective boundary layer. In *Atmospheric Turbulence and Air Pollution Modeling* (eds: *F.T.M. Nieuwstadt* and *H. van Dop*). D. Reidel Hingham, Mass.

Manton, M.J., 1975: Penetrative convection due to a field of thermals. *J. Atmos. Sci. 32*, 2272-2277.

Mitzeva, R., Evtimov, St. and *Doychinska, S.*, 1997: A one-dimensional thermal model of morning convective boundary layer development. *Időjárás 101*, 1-15.

Roache, P., 1976: *Computational Fluid Dynamics*. Hermosa Publisher, Albuquerque.

Stull, R. B., 1988: *An Introduction to Boundary Layer Meteorology*. Kluwer Academic Publisher, Dordrecht, Boston, London.

Stull, R.B., 1994: Fundamental processes in boundary layers. In *Proc. of a WCRP Workshop on the Parameterization of Sub-grid Scale Tracer Transport* (Virginia Beach, USA, 30 Nov-3 Dec 1993), WMO/TD- No. 823, 5-13.

Telford, J.W., 1966: The convective mechanism in clear air. *J. Atmos. Sci. 23*, 652-666.

Vulfson, N.T., 1961: *Convective Motion in a Free Atmosphere* (in Russian). Publ. Akad. Nauk, Moscow.

Warner, J. and *Telford, J.*, 1967: Convection below cloud base. *J. Atmos. Sci. 24*, 374-382.

IDŐJÁRÁS

Quarterly Journal of the Hungarian Meteorological Service
Vol. 104, No. 2, April–June 2000, pp. 123–136

Reconstruction of the spring temperatures in the 18th century based on the measured lengths of grapevine sprouts

Jaroslav Střeštík[1] and **József Verő**[2]

[1]*Geophysical Institute of the Academy of Sciences of the Czech Republic, Prague, Czech Republic*

[2]*Geodetical and Geophysical Research Institute of the Hungarian Academy of Sciences, H-9401 Sopron, P.O. Box 5, Hungary*

(Manuscript submitted for publication 26 October 1999; in final form 4 May 2000)

Abstract—Lengths of new grapevine sprouts, measured systematically in Kőszeg, Hungary, since 1740 on the same day of each year (24 April) exhibit a good correlation with the average air temperatures in April and in some extent in March. Weighted average (March + 2× April)/3 shows the best correlation, where the correlation coefficient reaches 0.6. Climatological data taken from Budapest, Vienna and Prague show that the correlation decreases with the increasing distance. Values higher by about 0.05 were obtained with square roots of the lengths instead of the proper lengths for all stations. All correlations between derivatives of the lengths and temperatures instead of original data are higher by 0.1. There is a negative correlation between these lengths and the relative air humidity or cloudiness. The correlation with precipitation, sunspot numbers and geomagnetic activity index is poor and not significant. These results confirm the relatively lower temperatures in the 19th century and the warm decades till the end of the 18th century, moreover, they suggest that the warm period continued back to the past at least till 1740; this statement is valid only for spring temperatures.

Key-words: temperature reconstruction, grapevine sprouts.

1. Introduction

Instrumental air temperature data series at individual stations are relatively short. Observations started at the most central European stations in the second half of the 18th century, e.g., at Prague-Klementinum in 1775, Vienna 1775, Budapest 1780, Munich 1781; longer series are available at Geneva from 1753, Basle 1755, DeBilt in The Netherlands 1716. At some stations the registration started earlier but it was later interrupted, e.g., at Berlin from 1706, but an uninterrupted series is available from 1756 only. All observed data used in this

paper originate from the database of *Bradley* (1992). Series with the length of 200 years or a little more render only few possibilities to determine and prove long-term trends or correlations with other sufficiently long observed series. Therefore respective conclusions concerning the possible climate development in future would not be sufficiently supported.

From this point of view it is very desirable to gain any guess of air temperature further to the past using various different observations or natural archives (e.g., *Jacoby* and *D'Arrigo*, 1989). Each of these reconstructions are, however, limited in some extent to the region where the data were taken from or the season connected with these data, and the accuracy is often different. One can claim that independent reconstructions of climate for the period before the instrumental observation are always desirable.

2. Measurements

In this paper we shall use the measured lengths of new grapevine sprouts. These lengths have been systematically measured since 1740 in Kőszeg for different grapevine varieties and in different localities in the vicinity of the town, on the same day of each year (24 April). Kőszeg is situated in West Hungary near the boundary with Austria, where the long Pannonian basin changes into low mountains (last parts of the Alps). Though this is not as famous wine region as other Hungarian ones, inhabitants keep an interesting tradition: every year on St. George's day (24 April) a procession in folk costumes moves through the town bringing new grapevine sprouts from vineyards in the vicinity of the town to the town hall. These sprouts are then drawn on paper as documentation, keeping carefully their size and form. These pictures have been saved in the town museum since 1740 till now.

Till 1868 all drawings were prepared by Indian ink, later completed by colours, and by coloured photos in real size from 1962. Together with them, some information are saved about the wine production. They have not a big meaning because there are not always the data of the vineyard area. Moreover, there are some comments concerning the weather, especially unusual meteorological occasions. E.g., in 1929 it was mentioned that a severe winter occurred in February (on February 11, 1929 the lowest temperature in the Czech Republic was recorded) when many grapevine varieties were destroyed by frost causing significantly lower production. All these comments are written in Hungarian by hand, some older ones are not well legible.

The lengths of the mentioned grapevine sprouts are very different. In some years only not yet opened blossoms could be found on the branches, whereas in other years new branches could grow more than 30 cm till the 24th of April. The paintings have been saved for two centuries in the museum and perhaps nobody, not living in the town, knew about them. At the end of the thirties of

the 20th century *Aladár Visnya*, the director of the museum, measured all these painted sprouts and offered them to the Meteorological Institute in Budapest. *Zoltán Berkes*, a meteorologist, compared these lengths to the observed air temperatures in Budapest and Vienna. Results were published in Hungarian and German (*Berkes*, 1942). *Péczely* (1982) carried out a correlation analysis with average temperatures and sunshine duration in March and April, and obtained a rather close quadratic connection with spring temperatures. The results of Berkes and Péczely showed some interesting correlations. The data are by 60 years longer now and represent a very valuable material for further investigations.

3. Results

Lengths of grapevine sprouts for 1740–1939 are published in *Berkes* (1942). Lengths for 1900–1998 were measured in the original paintings in the Kőszeg museum (years 1900–1939 for comparison with Berkes' measurements). Visitors can see some of them. All the lengths for 259 years are given in *Table 1*. Besides the original paintings there are copies of smaller size (1:4) available, these are too small and were not used. The lengths in the individual years are graphically represented in *Fig. 1*. Striking low values after 1900 can be distinguished at the first view, it will be explained later.

In his paper *Berkes* gives attention to some inhomogeneities, which could decrease the accuracy of the results found. The measurements have been done on the same day of each year, in this point no objection can be risen. But there are different grapevine varieties, some of them grow earlier and the others later. The sprouts were taken from different localities in the vicinity of the town with possible different microclimate. Fortunately, more sprouts have been documented each year (at least five or often more) and the grapevine variety and locality have always been assigned. The most frequently planted and in museum documented ones are Burgund and Blue Frankos. Their sprouts have usually equal length. *Berkes* used only these varieties. If in some (not numerous) years these varieties were not documented, *Berkes* used other varieties (e.g., the third most frequently used Riesling) and comparing its length with the lengths of other varieties in other years he guessed the corresponding length of Burgund. The most serious inhomogeneity occurred in 1900. In this year the vineyards were attacked by Phyloxera, therefore it was necessary to cut old plants and to introduce new variants. They grow slower than the older ones and this is the explanation of systematically shorter branches in the 20th century.

Berkes compared the measured grapevine sprout lengths with the observed air temperatures in Budapest and Vienna. Temperatures measured directly in Kőszeg are available only for a short recent period. For all variants of temperatures (described later) the correlation with the data of Budapest was higher than with Vienna data. Vienna is nearer, but climatologically it is a bit

different from Budapest or Kőszeg. *Berkes* also used data from Prague (Klementinum). He considers them of high quality. Of course, due to the longer distance the correlation with Prague data is worse but still significant.

Table 1. Lengths of grapevine sprouts in centimetres measured in Kőszeg on April 24, each year. The table continues with the corrected data since 1900.
A – multiplied by two, B – multiplied by three. Data till 1940 are taken from *Berkes* (1942)

	Year	0	1	2	3	4	5	6	7	8	9
	1740	0	1	0	1	7	21	0	4	1	4
	1750	27	3	11	12	4	28	6	31	1	6
	1760	8	28	12	5	3	5	20	0	6	14
	1770	0	0	0	0	20	21	9	5	9	48
	1780	4	20	0	13	3	0	0	0	5	0
	1790	0	0	2	0	8	0	2	17	33	0
	1800	2	6	5	0	3	0	5	0	2	0
	1810	0	13	0	7	25	9	7	0	5	20
	1820	10	6	11	10	0	3	18	12	17	9
	1830	17	14	8	0	4	5	8	0	0	0
	1840	5	13	3	14	14	0	13	0	20	1
	1850	8	15	1	0	15	4	12	9	0	9
	1860	0	3	20	12	1	7	18	1	4	13
	1870	1	7	7	12	8	1	18	1	10	5
	1880	6	1	9	0	6	9	1	2	3	3
	1890	11	1	6	15	26	2	2	11	8	4
	1900	1	3	1	1	11	4	12	1	1	3
	1910	3	5	1	1	5	5	2	1	5	2
	1920	2	6	2	2	4	2	2	2	3	0
	1930	2	1	1	1	10	2	3	1	4	2
	1940	2	1	1	4	1	10	2	3	4	3
	1950	3	1	4	6	0	1	1	3	0	7
	1960	3	10	1	3	2	1	4	3	3	1
	1970	1	2	2	1	8	2	4	1	1	2
	1980	1	3	1	2	1	2	1	2	1	9
	1990	5	1	2	1	6	3	0	0	2	
(A)	1900	2	6	2	2	22	8	24	2	2	6
	1910	6	10	2	2	10	0	4	2	10	4
	1920	4	11	4	3	8	3	4	3	4	0
	1930	2	1	1	1	23	3	5	2	8	4
	1940	2	2	1	8	2	19	4	5	8	6
	1950	6	2	8	11	0	1	1	5	0	14
	1960	6	20	2	5	4	2	7	5	5	1
	1970	1	4	4	2	15	3	8	2	2	4
	1980	1	5	2	4	2	4	2	3	2	18
	1990	9	2	3	2	11	5	0	0	4	
(B)	1900	3	9	3	3	33	12	36	3	3	9
	1910	9	15	3	3	15	15	6	3	15	6
	1920	7	16	6	4	12	5	6	5	6	0
	1930	4	2	2	2	34	4	7	2	11	6
	1940	4	3	2	12	3	28	7	8	12	9
	1950	8	3	12	16	0	2	2	8	0	21
	1960	9	30	3	8	6	3	10	8	8	2
	1970	2	6	7	3	22	4	12	3	3	5
	1980	3	8	3	7	3	5	3	4	4	27
	1990	14	3	4	4	16	8	0	0	7	

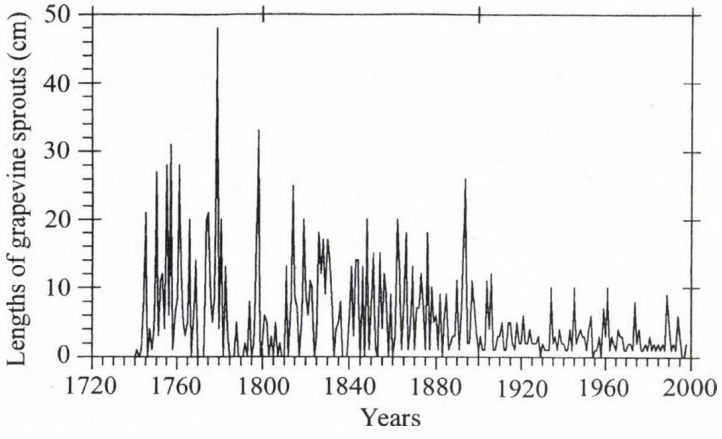

Fig. 1. Lengths of grapevine sprouts in the individual years in centimetres.

The highest correlation appeared for average temperatures in March + April of the current year: for Budapest it is 0.70 and for Vienna 0.58. With respect to the possible inhomogeneity around 1900 he calculated the correlations separately till 1899. In this case the coefficients were even higher: 0.77 for Budapest and 0.63 for Vienna. Using monthly averages only for April he arrived to little lower values: only 0.62 for Budapest. The level of the 99% significance is 0.20 for his 160 year series (i.e., 1740–1899). The correlation with temperatures in other months (February, etc.) were insignificant. Correlation with the precipitation (data series from Budapest were only 80 years long) was on the significance level (–0.21). The more rainy weather is usually colder. *Berkes* found a possible correlation with solar activity; the coefficient is about 0.26.

Series longer by 60 years can bring more accurate results. We shall use some extended combination of climatological data. The purpose is to find how the different kinds of weather influence the growth of grapevine sprouts in spring. In other words, we want to know precisely what the results tell us and what we have reconstructed from the measured lengths. The most important correlation coefficients are summarised in *Table 2*. With respect to a possible inhomogeneity around 1900 first we calculated the correlation with Budapest temperature separately for periods till 1900 and from 1901, and then for the whole period and other stations. Levels for the 99% significance of correlation coefficients are 0.20 for the first part, 0.26 for the second part and 0.16 for the whole period. In columns we found correlations with average temperatures in March (III), April (IV), March + April (A) and with weighted average where temperatures in April were taken with double weight than in March (WA). For

the latter combination the highest values were obtained. Temperatures in April influence the growth surely more than in March. As a whole, all correlations are lower than those mentioned by *Berkes*, including periods used by him. *Berkes* probably used average April temperatures only till 24 April instead of the whole month. This calculation is methodically better. However, we are able to repeat this calculation for data of Prague only. These results are written in the last row of Table 2 and marked by Prague G (the same notation is used in other tables). Correlation coefficients calculated for these means are really higher than for the whole month. Correlations with average temperatures in February move between 0.10 and 0.15 being under the 95% significance level. Other combinations of months also result in somewhat lower values than those in the last column of Table 2. Further, in contrary to *Berkes*, there are relatively small differences between coefficients for Budapest and Vienna, and even for Prague we have obtained high values. Correlations were calculated for some other stations, e.g., for Klagenfurt or Geneva. They decrease with the increasing distance, however, for stations mentioned they are still significant.

Table 2. Correlation of lengths of grapevine sprouts with mean air temperatures—original data. Lower part of the table expresses the correlations between derivatives of the data

Station	Period	III	IV	A	WA
Budapest	1780–1900	0.395	0.516	0.598	0.613
Budapest	1901–1998	0.347	0.425	0.508	0.529
Budapest	1780–1998	0.178	0.447	0.405	0.466
Wien	1775–1998	0.186	0.393	0.378	0.422
Prague	1775–1998	0.221	0.371	0.367	0.394
Prague G	1775–1998		0.422	0.403	0.437
Budapest	1780–1900	0.441	0.552	0.615	0.625
Budapest	1901–1998	0.395	0.516	0.597	0.613
Budapest	1780–1998	0.347	0.422	0.499	0.522
Wien	1775–1998	0.390	0.528	0.587	0.608
Prague	1775–1998	0.335	0.473	0.518	0.539
Prague G	1775–1998		0.520	0.552	0.578

Lower lengths after 1900, well observed in Fig. 1, offer a possibility to introduce some corrections and homogenization of the data. We tried to multiply all values after 1900 by two or three. For this purpose we used values directly measured with the accuracy of 0.2 cm, not the published ones (also in Table 1) in cm, so the corrected values are not always simple multiples of the original values. These corrected lengths are given in the lower part of Table 1 (multiplication by 2 is marked by A, by 3 is marked by B. The same notation is used in the other tables.). Correlation coefficients for both corrections and

the temperatures in different months are given in *Table 3*. It seems that multiplication by three results in higher coefficients as a whole and seems therefore more suitable. The corrected data are represented in *Fig. 2* together with the smoothed course.

Table 3. Correlation of lengths of grapevine sprouts with mean air temperatures—corrected data. Lower part of the table expresses the correlations between derivatives of the data

Station	Kőszeg data	III	IV	A	WA
Budapest	corr. A	0.283	0.468	0.501	0.543
Budapest	corr. B	0.338	0.441	0.528	0.551
Wien	corr. A	0.279	0.427	0.469	0.500
Wien	corr. B	0.333	0.423	0.508	0.525
Prague	corr. A	0.302	0.422	0.454	0.478
Prague	corr. B	0.350	0.440	0.510	0.494
Prague G	corr. A		0.478	0.492	0.519
Prague G	corr. B		0.494	0.534	0.554
Budapest	corr. A	0.452	0.545	0.635	0.649
Budapest	corr. B	0.435	0.540	0.620	0.638
Wien	corr. A	0.415	0.551	0.618	0.638
Wien	corr. B	0.414	0.546	0.615	0.635
Prague	corr. A	0.356	0.503	0.551	0.572
Prague	corr. B	0.358	0.511	0.557	0.579
Prague G	corr. A		0.520	0.552	0.578
Prague G	corr. B		0.540	0.583	0.611

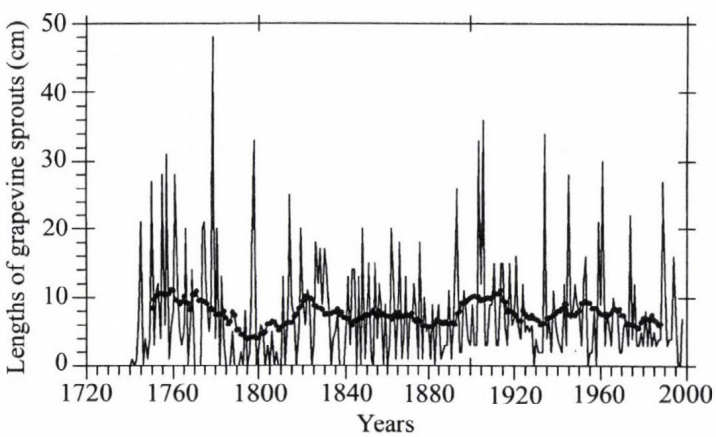

Fig. 2. Lengths of grapevine sprouts in the individual years in centimetres with correction B. Smoothed data—running averages in the 21 year interval— are drawn by thick line.

Introducing a correction for the data after 1900 improves the correlations. Nevertheless, the correlations in the 20th century are always lower than those before 1900. This is caused by the fact that the rapid increase in temperatures during the last decade does not have a corresponding response in the lengths of grapevine sprouts. Using an interval, e.g., 1901–1990 instead of 1901–1998, one arrives to little higher values. It seems therefore that the grapevine sprout lengths reflect the short-time fluctuations more than the long-term trend. Any attempt to separate these two factors (even drawing the long-term trend by hand!) brings higher correlations for the data where the long-term trend was removed, and poor correlations for the long-term trends themselves as well. This regularity is better seen using the derivatives of all data series instead of the original data (i.e., the increase of temperatures and grapevine sprouts lengths with respect to the previous year). All these correlations are given in the second part of Table 2 and the same will be done in all following tables. It is clear that the correlation is higher by about 0.1. Correlations of derivatives of lengths with temperatures (and vice versa) are significantly lower.

Using correlation coefficients one silently supposes that the relation between correlated quantities is linear. In this case this point is not quite satisfied. It is clear that the growth is very slow at the beginning and the spouts only later grow more rapidly. So the difference at the lengths 0 or 1 cm corresponds to a relatively serious difference in temperature whereas there is no such a difference between the lengths 30 or 35 cm. Therefore it is better to correlate the temperature not with the length of sprouts but, e.g., with its logarithm or square root, etc. This transformation decreases the differences between long sprouts (20, 30, 40 cm). We decided for square roots rather than logarithms because of difficulties with zero lengths. The second reason to introduce this transformation was that the grapevine sprout lengths do not exhibit normal distribution (for the temperatures the situation is better). After the transformation the distribution is nearer to the normal one. Correlation coefficients between square roots of grapevine sprout lengths and the same temperatures as in Tables 2 and 3 are given in *Table 4*. In *Fig. 3* a correlation between these square roots for data with correction B and the weighted average of March and April temperature in Budapest are shown. It is clear that with this transformation the relation is nearly linear. Using logarithm instead of square root brings the same result (one must define a value for the zero length). Correlation between derivatives is higher than that for original data also in the case of square roots.

In Fig. 3, on its left side, a small separate group of points can be distinguished. They correspond to the zero sprout length and usually to low temperatures. In these years one may hardly discuss the correlation between sprout lengths and anything else. The same figure prepared without this group shows clearer dependence. The coefficient does not increase significantly but the regression line is steeper. It seems that it has a meaning to exclude years

with zero sprout lengths. The regression line in Fig. 3 can be expressed by the formula $T=0.630\ d^{-2}+6.08$, where T is the temperature used in Fig. 2 and d is the length of grapevine sprouts. Without the group with zero lengths the relation is $T=0.650\ d^{-2}+5.96$.

Table 4. Correlation of square roots of lengths of grapevine sprouts with mean air temperatures—original and corrected data B.
Lower part of the table expresses the correlations between derivatives of the data

Station	Kőszeg data	III	IV	A	WA
Budapest	no corr.	0.204	0.491	0.452	0.517
Budapest	corr. B	0.376	0.498	0.592	0.619
Wien	no corr.	0.217	0.429	0.422	0.468
Wien	corr. B	0.375	0.467	0.566	0.584
Prague	no corr.	0.303	0.439	0.464	0.486
Prague	corr. B	0.411	0.490	0.569	0.577
Prague G	no corr.		0.483	0.495	0.524
Prague G	corr. B		0.539	0.601	0.617
Budapest	no corr.	0.460	0.572	0.656	0.674
Budapest	corr. B	0.468	0.591	0.672	0.694
Wien	no corr.	0.452	0.596	0.670	0.692
Wien	corr. B	0.465	0.606	0.686	0.708
Prague	no corr.	0.426	0.551	0.630	0.645
Prague	corr. B	0.438	0.575	0.653	0.669
Prague G	no corr.		0.584	0.655	0.673
Prague G	corr. B		0.603	0.674	0.693

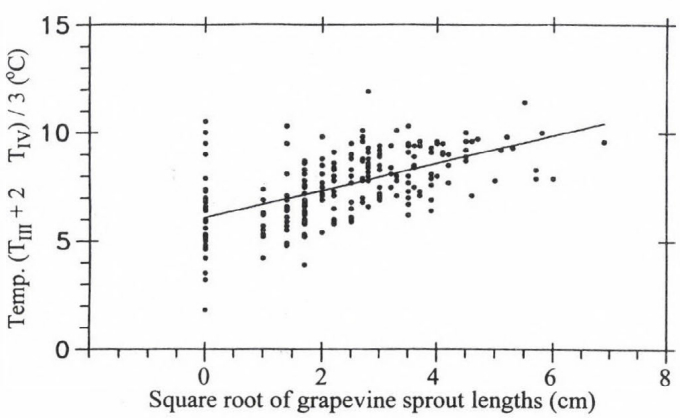

Fig. 3. Correlation of the square roots of lengths of grapevine sprouts with weighted averages of March and April temperatures in Budapest.

Till now only the monthly mean temperatures were used. In the Prague Klementinum series the daily maxima and morning minima have been available since 1775. Their monthly means were calculated and these means were used for correlation with the measured sprout lengths. All combinations of temperatures including April means till April 24 (marked with Prague G) were used. All correlation coefficients are also given in *Tables 5* and *6* for corrected lengths marked with "corr. B". Correlations are also given for square roots (marked with "sq"). When compared with monthly means for Prague corr. B in Tables 3 and 4 it is seen that the correlations are a bit higher for maximal temperatures than for daily means and especially for morning minimal temperatures. It is very probable that also for Budapest and Vienna the correlation with maximal temperatures would be a bit higher than for daily means.

Table 5. Correlation of lengths of grapevine sprouts and their square roots with maximal air temperatures—original and corrected data B.
Lower part of the table expresses the correlations between derivatives of the data

Station	Kőszeg data	III	IV	A	WA
Prague	no corr.	0.203	0.344	0.343	0.369
Prague	corr. B	0.353	0.443	0.446	0.515
Prague	no corr. sq.	0.286	0.416	0.443	0.464
Prague	corr. B sq.	0.413	0.495	0.578	0.585
Prague G	no corr.		0.391	0.376	0.405
Prague G	corr. B		0.495	0.540	0.555
Prague G	no corr. sq.		0.458	0.473	0.497
Prague G	corr. B sq.		0.545	0.610	0.623
Prague	no corr.	0.348	0.486	0.542	0.559
Prague	corr. B	0.374	0.531	0.587	0.607
Prague	no corr. sq.	0.442	0.557	0.651	0.660
Prague	corr. B sq.	0.454	0.585	0.677	0.689
Prague G	no corr.		0.543	0.581	0.605
Prague G	corr. B		0.577	0.621	0.645
Prague G	no corr. sq.		0.599	0.680	0.694
Prague G	corr. B sq.		0.623	0.704	0.718

For comparison of the grapevine sprout lengths with precipitation data in March and April not sufficiently long series are available from stations near Kőszeg. The nearest station with longer series is Klagenfurt (starting in 1813), Kremsmünster (1820), Prague (1805), Geneva (1826), and perhaps Budapest

(1841). Calculating the same correlations as for temperatures we have found no correlation better than 0.1, and this value is much under the significance level.

Table 6. Correlation of lengths of grapevine sprouts and their square roots with minimal air temperatures—corrected data B.
Lower part of the table expresses the correlations between derivatives of the data

Station	Kőszeg data	III	IV	A	WA
Prague	no corr.	0.308	0.354	0.417	0.425
Prague	corr. B sq.	0.374	0.413	0.497	0.506
Prague G	corr. B		0.397	0.441	0.455
Prague G	corr. B sq.		0.457	0.522	0.534
Prague	corr. B	0.297	0.416	0.452	0.476
Prague	corr. B sq.	0.307	0.442	0.475	0.500
Prague G	corr. B		0.456	0.475	0.501
Prague G	corr. B sq.		0.471	0.492	0.519

Comparison with the mean cloudiness or the relative air humidity gives more chance. Cloudiness data from Prague are available from 1775, humidity data only from 1845. Correlation coefficients between sprout lengths and monthly means of cloudiness and relative humidity are given in *Table 7*, arranged in the same way as in Table 6. Values in some columns exceed the 99% significance level, in other at least the 95% level. Nearly zero values for March reflect themselves in lower values for periods that include March (columns A and WA), while the correlation with April data alone is higher than in columns A and WA. Here we can observe a bit higher correlation for square roots again, showing that also in this case the dependence is not linear. Correlation coefficients are negative. The cause is that higher cloudiness and relative humidity in these months are connected with colder weather. The 99% significance level is 0.16 for the cloudiness results and 0.21 for the humidity results. It should be stressed that in the case of cloudiness and relative humidity no increase in correlation coefficients has been found using correction of the lengths after 1900, the values are nearly the same.

As to solar activity, monthly means of sunspot numbers are available for the whole period, but their correlation with the measured lengths is very low. For any combination of months as used for temperatures, for all corrections and using square roots all values are not higher than 0.1, more often only about 0.05, being very much under the 95% significance limit. For geomagnetic activity, where the index aa is available from 1868, the coefficients do not exceed 0.13, however, in this case the 99% significance limit is 0.25.

Table 7. Correlation of lengths of grapevine sprouts with some other quantities—corrected data B. Lower part of the table expresses the correlations between derivatives of the data

Quantity	III	IV	A	WA
Prague, rel. humidity	-0.003	-0.242	-0.073	-0.114
Prague G, rel. humidity		-0.160	-0.091	-0.129
Prague, cloudiness	-0.120	-0.338	-0.275	-0.312
Prague, G. cloudiness		-0.351	-0.292	-0.327
Klagenfurt, precipit.	-0.050	-0.111	.0.108	-0.115
Wolf sunspot number	-0.049	-0.030	-0.040	-0.037
Geomagnetic aa index	-0.124	-0.113	-0.129	-0.126
Prague, rel. humidity	-0.211	-0.206	-0.229	-0.228
Prague G, rel. humidity		-0.209	-0.258	-0.246
Prague, cloudiness	-0.260	-0.291	-0.315	-0.348
Prague, G. cloudiness		-0.363	-0.371	-0.377
Klagenfurt, precipit.	-0.013	-0.026	-0.026	-0.027
Wolf sunspot number	-0.007	0.057	0.027	0.039
Geomagnetic aa index	-0.084	-0.036	-0.071	-0.060

4. Conclusion

To conclusion we shall represent graphically the course of the air temperature in Budapest (weighted averages for March+April=WA used in tables) together with the square roots of the lengths of grapevine sprouts (this combination exhibits the best correlation), both smoothed by running averages in 21 year interval (*Fig. 4*). The picture shows good agreement between the curves. Both curves display similar periods with higher or lower values lasting for several decades, with the exception of the last decades (after 1960). This point confirms other observed and indirect data. The sprouts were relatively long even in decades before 1780 (see Figs. 1 and 4), where no instrumental observation in the region in question was available. We may judge that spring temperatures between 1740–1780 were approximately on the same level as between 1780–1790, whilst they were surely higher than those in the middle of the 19th century.

This result agrees well with the reconstructed course of temperatures received by *Jacoby* and *D'Arrigo* (1989) and based on the tree-rings from the arctic regions. They also found a clear maximum at the end of the 18th and the beginning of the 19th century, which continues with some fluctuations more to the past, with some short-time maxima during 1720–1780. A deeper minimum appears between 1700–1720 but not so deep as that in the 19th century. The correlation coefficient is very low between the temperatures given by *Jacoby* and *D'Arrigo* and the sprout lengths. This is probably due to the relatively stable sprout lengths in the 20th century, when the temperature permanently increases, and due to the big year-to-year fluctuation of the lengths compared with a smooth course of reconstructed temperatures. For corrected data (corr.

B) one arrives to higher correlations, nevertheless, they are still under the significance level. Better results can be obtained for smoothed data (running averages in 21 year interval). For corrected data of sprouts the correlation coefficient reaches 0.15.

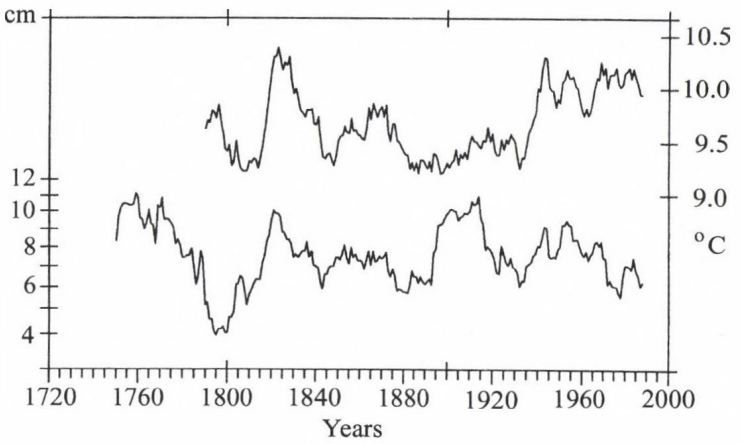

Fig. 4. Course of spring temperatures in Budapest (weighted average March+2 × April) —shown by the upper curve and the right-hand scale. Lengths of grapevine sprouts in Kőszeg—shown by the lower curve and the left-hand scale. Both courses are smoothed using running averages in the 21 year interval.

Low correlation with the data from *Jacoby* and *D'Arrigo* does not mean that the results from grapevine sprout lengths are wrong. Data used for comparison originate from quite different regions and because they are based on tree-rings they include the whole period of vegetation. Grapevine sprouts data, on the other hand, originate from Hungary and are influenced only by the spring temperatures till 24 April, they cannot be influenced by summer temperatures. So we have reconstructed a different kind of data, for a special month. We confirmed high spring temperatures at the end of the 18th century continuing at least till 1740, speaking nothing of summer or winter temperatures in the years in question. The approximately 200 year wave, apparent in the 1780–1980 data, is not so obvious before 1740, at least for spring temperatures, and the natural climate fluctuations are more complicated than it was thought earlier.

Acknowledgements—The authors wish to express their thanks to *Dr. Kornél Bakay*, Director of the Kőszeg Museum who kindly enabled us to provide measurements of the original pictures of grapevine sprouts saved in the museum.

References

Berkes, Z., 1942: Reflection of climate variability in the length of Kőszeg grapevine sprouts (in Hungarian and German). *A Magyar Királyi Földmivelésügyi Minisztérium fennhatósága alatt álló Magyar Kir. Orsz. Meteorológiai és Földmágnességi Intézet kisebb kiadványai, új sorozat 15. szám*, S. 3-17.

Bradley, R., 1992: Climate since AD 1500 Database. IGBP PAGES/World Data Center-A for Paleoclimatology Data Contribution Series # 92-015.

Jacoby, G. C. and *D'Arrigo, R.*, 1989: Reconstructed Northern Hemisphere annual temperature since 1671 based on a high-latitude tree-ring data from North America. *Climatic Change 14*, 39-45 (available also on Internet).

Péczely Gy., 1982: The "Kőszeg Book of grapevine sprouts" (in Hungarian). *Légkör 27*, No. 3, 24-27.

BOOK REVIEWS

Henning Rodhe and Robert Charlson (editors): **The Legacy of Svante Arrhenius Understanding the Greenhouse Effect**. Royal Swedish Academy of Sciences & Stockholm University, 1998. 212 pages.

In April 1896, the Swedish scientist Svante Arrhenius, who was later awarded the Nobel Prize for his outstanding work in the field of chemistry, published a paper in *The Philosophical Magazine* which is still frequently cited in the scientific literature. His work entitled "On the Influence of Carbonic Acid in the Air upon the Temperature of the Ground" made the first attempt to quantify the greenhouse effect caused by atmospheric carbon dioxide of anthropogenic origin. It is not an overstatement to say that the contemporary climate change research is based on this paper. He assumed, a 50% increase in the atmospheric mixing ratio of carbon dioxide would take about 3000 years, but now we know, if the present tendency will not change significantly, that level will be reached before the middle of the new century.

In order to commemorate the centenary of the publication of Arrhenius' paper, the Royal Swedish Academy of Sciences and the International Meteorological Institute in Stockholm organised a workshop on 9–10 April 1996. The book contains the presentations of the workshop. Each chapter/presentation is followed by a remarkable list of references.

The authors of the first chapters of the book review the state-of-the-art of science in the era of Arrhenius and the scientific context of his work. Originally, he intended to explain the formation of the Ice Ages, but nowadays his work is mostly cited in papers covering the global warming issue.

Several further papers discuss the historical development in certain fields of the atmospheric greenhouse effect. Thus, among others, the reader can learn how our knowledge got richer on the global carbon cycle, on the climate forcing of the aerosol particle, and on the greenhouse effect itself. We can get acquainted with the development of the climate models and with the numerical simulations of anthropogenic climate change. In addition to the historical reviews of the topics, the newest results illustrated by impressive colour figures can also be found in the chapters.

The last two presentations lead us on to the field of social sciences. How can the climate affect the human civilisation and what do people know about the climate change issue? What was the relation between Science and Policy 100 years ago and what is it like today?

And, as the last chapter of the book, one can find the facsimile copy of the famous paper of Svante Arrhenius.

The book reviewing the research of the atmospheric greenhouse effect from the beginning to our day can be recommended for both graduate students and research workers in geosciences. It can also be recommended to all educated persons interested in the history of science or in the global climate change issue. The book is available from the publisher.

László Haszpra

L. Göőz: **On the natural resources. Natural resources of Szabolcs-Szatmár-Bereg county** (in Hungarian with English and German summaries). Grafit Press Ltd, Nyíregyháza, 1999, pp. 374, 112 figures, several colour photos, 86 tables.

This book provides a comprehensive survey of the complexity of various resources as well as a summary of the author's scientific activity during the recent three decades. The book consists of ten chapters.

The first chapter deals with the principles of research of natural resources including the definition of the natural resource, the use of the geographic information system (GIS), the aim and methods of regional investigations in Szabolcs-Szatmár-Bereg (Sz-Sz-B) county (the north-east part of Hungary).

In the second chapter the author summarizes the geological structure and mineral possessions of Sz-Sz-B county, emphasizing the stores of oil, coal and natural gas, while the third chapter describes the energy production on the base of sustainable development. In this chapter he gives precious data on energy consumption with different sources of power in Sz-Sz-B county.

The fourth chapter gives characterization on water stores and water management of the county, while the fifth chapter deals with the agricultural potentiality in the region of Sz-Sz-B county.

The sixth chapter provides a summary of the geothermal resources of the county, and gives most recent data on output of thermal water from 27 springs, besides on chemical constituents of the mineral waters in several wells as well as utilization of the thermal water in heating of households.

The seventh chapter is dedicated to the problems of the possible utilization of the atmospheric resources, like solar and wind energy ; the author gives a good survey on radiation and wind climate of the county.

The last three chapters deal with biomass as natural resource, the relationship between the environment and the use of the natural resources and the decision strategy in the exploitation of different renewable resources.

About 360 books and papers are cited.

Finally, the author attaches appendix with data on stores of important minerals, ores, water chemistry, etc.

György Koppány

ATMOSPHERIC ENVIRONMENT

an international journal

To promote the distribution of Atmospheric Environment *Időjárás* publishes regularly the contents of this important journal. For further information the interested reader is asked to contact *Prof. P. Brimblecombe*, School for Environmental Sciences, University of East Anglia, Norwich NR4 7TJ, U.K.; E-mail: atmos_env@uea.ac.uk

Volume 34 Number 2 2000

X. Querol, A. Alastuey, A. Chaves, B. Spiro, F. Plana and *A. Lopez-Soler:* Sources of natural and anthropogenic sulphur around the Teruel power station, NE Spain. Inferences from sulphur isotope geochemistry, 333-345.

Volume 34 Number 3 2000

A.S. Lefohn: Atmospheric sciences and applications to air quality, 351-351.

H. Ueda, T. Takemoto, Y.P. Kim and *W. Sha:* Behaviors of volatile inorganic components in urban aerosols, 353-361.

D.G. Streets and *S.T. Waldhoff:* Present and future emissions of air pollutants in China: SO2, NOx, and CO, 363-374.

S.J. Lindley, D.E. Conlan, D.W. Raper and *A.F.R. Watson:* Uncertainties in the compilation of spatially resolved emission inventories - evidence from a comparative study, 375-388.

J. Ma and *X. Zhou:* Development of a three-dimensional inventory of aircraft NO_x emissions over China, 389-396.

B. Owen, H.A. Edmunds, D.J. Carruthers and *R.J. Singles:* Prediction of total oxides of nitrogen and nitrogen dioxide concentrations in a large urban area using a new generation urban scale dispersion model with integral chemistry model, 397-406.

J. Saltbones, A. Foss and *J. Bartnicki:* Threat to Norway from potential accidents at the Kola nuclear power plant. Climatological trajectory analysis and episode studies, 407-418.

S.H. Ye, W. Zhou, J. Song, B.C. Peng, D. Yuan, Y.M. Lu and *P.P. Qi:* Toxicity and health effects of vehicle emissions in Shanghai, 419-429.

T. Sakai, T. Shibata, S.A. Kwon, Y.S. Kim, K. Tamura and *Y. Iwasaka:* Free tropospheric aerosol backscatter, depolarization ratio, and relative humidity measured with the Raman lidar at Nagoya in 1994-1997: contributions of aerosols from the Asian Continent and the Pacific Ocean, 431-442.

Q. Zhiqiang, K. Siegmann, A. Keller, U. Matter, L. Scherrer and *H.C. Siegmann:* Nanoparticle air pollution in major cities and its origin, 443-451.

J. Hao, D. He, Y. Wu, L. Fu and *K. He:* A study of the emission and concentration distribution of vehicular pollutants in the urban area of Beijing, 453-465.

P. Thunis and *C. Cuvelier:* Impact of biogenic emissions on ozone formation in the Mediterranean area — a BEMA modelling study, 467-481.

M.J. Phadnis and *G.R. Carmichael:* Forest fire in the Boreal Region of China and its impact on the photochemical oxidant cycle of East Asia, 483-498.

H.A. Bravo and *R.J. Torres:* The usefulness of air quality monitoring and air quality impact studies before the introduction of reformulated gasolines in developing countries. Mexico City, a real case study, 499-506.

R. Bornstein and *Q. Lin:* Urban heat islands and summertime convective thunderstorms in Atlanta: three case studies, 507-516.

Volume 34 Number 4 2000

S.I. Fujita, A. Takahashi, J.H. Weng, L.F. Huang, H.K. Kim, C.K. Li, F.T.C. Huang and *F.T. Jeng:* Precipitation chemistry in East Asia, 525-537.

M. Sharan, S.G. Gopalakrishnan, R.T. Mcnider and *M.P. Singh:* A numerical investigation of urban influences on local meteorological conditions during the Bhopal gas accident, 539-552.

Y. Tsutsumi and *H. Matsueda:* Relationship of ozone and CO at the summit of Mt. Fuji (35.35°N, 138.73°E, 3776 m above sea level) in summer 1997, 553-561.

B.K. Lee, S.H. Hong and *D.S. Lee:* Chemical composition of precipitation and wet deposition of major ions on the Korean peninsula, 563-575.

P.K. Padhy and *C.K. Varshney:* Total non-methane volatile organic compounds (TNMVOC) in the atmosphere of Delhi, 577-584.

S. Cheng and *K.C. Lam:* Synoptic typing and its application to the assessment of climatic impact on concentrations of sulfur dioxide and nitrogen oxides in Hong Kong, 585-594.

J.Y. Kim, Y.S. Ghim, Y.P. Kim and *D. Dabdub:* Determination of domain for diagnostic wind field estimation in Korea, 595-601.

Q. Jinhuan and *Y. Liquan:* Variation characteristics of atmospheric aerosol optical depths and visibility in North China during 1980-1994, 603-609.

C.S. Li and *Y.S. Ro:* Indoor characteristics of polycyclic aromatic hydrocarbons in the urban atmosphere of Taipei, 611-620.

S. Seto, M. Oohara and *Y. Ikeda:* Analysis of precipitation chemistry at a rural site in Hiroshima Prefecture, Japan, 621-628.

R. Mondal, G.K. Sen, M. Chatterjee, B.K. Sen and *S. Sen:* Ground level concentration of nitrogen oxides (NOx) at some traffic intersection points in Calcutta, 629-633.

Australasias

H.B. Singh, W. Viezee, Y. Chen, J. Bradshaw, S. Sandholm, D. Blake, N. Blake, B. Heikes, J. Snow, R. Talbot, E. Browell, G. Gregory, G. Sachse and *S. Vay:* Biomass burning influences on the composition of the remote South Pacific troposphere: analysis based on observations from PEM-Tropics-A, 635-644.

C. He, F. Murray and *T. Lyons:* Monoterpene and isoprene emissions from 15 *Eucalyptus* species in Australia, 645-655.

M.W. Priest, D.J. Williams and *H.A. Bridgman:* Emissions from in-use lawn-mowers in Australia, 657-664.

M.J.R. Halstead, R.G. Cunninghame and *K.A. Hunter:* Wet deposition of trace metals to a remote site in Fiordland, New Zealand, 665-676.

Antarctica

D.H. Lowenthal, J.C. Chow, D.M. Mazzera, J.G. Watson and *B.W. Mosher:* Aerosol vanadium at McMurdo Station, Antarctica: implications for Dye 3, Greenland, 677-679.

Volume 34 Number 5 2000

M.D. King, E.M. Dick and *W.R. Simpson:* A new method for the atmospheric detection of the nitrate radical (NO_3), 685-688.

H. Huang, Y. Akutsu, M. Arai and *M. Tamura:* A two-dimensional air quality model in an urban street canyon: evaluation and sensitivity analysis, 689-698.

A. Samanta and *L.A. Todd:* Mapping chemicals in air using an environmental CAT scanning system: evaluation of algorithms, 699-709.

A. Prieme, T.B. Knudsen, M. Glasius and *S. Christensen:* Herbivory by the weevil, *Strophosoma melanogrammum*, causes severalfold increase in emission of monoterpenes from young Norway spruce (*Picea abies*), 711-718.

R.C. Musselman and *T.J. Minnick:* Nocturnal stomatal conductance and ambient air quality standards for ozone, 719-733.

NOTES TO CONTRIBUTORS OF *IDŐJÁRÁS*

The purpose of the journal is to publish papers in any field of meteorology and atmosphere related scientific areas. These may be

- reports on new results of scientific investigations,
- critical review articles summarizing current state of art of a certain topic,
- shorter contributions dealing with a particular question.

Each issue contains "News" and "Book review" sections.

Authors may be of any nationality, but the official language of the journal is English. Papers will be reviewed by unidentified referees.

Manuscripts should be sent to
Editor-in-Chief of IDŐJÁRÁS
P.O. Box 39
H-1675 Budapest, Hungary

in three copies including all illustrations. One set of illustrations has to be of camera ready quality, the other two might be lower quality.

Title part of the paper should contain the concise title, the name(s) of the author(s), the affiliation(s) including postal and E-mail address(es). In case of multiple authors, the cover letter should indicate the corresponding author.

Abstract should follow the title, it contains the purpose, the data and methods as well as the basic conclusion.

Key-words are necessary to help to classify the topic.

The text has to be typed in double spacing with wide margins. Word-processor printing is preferred. The use of SI units are expected. The negative exponent is preferred to solidus. Figures and tables should be consecutively numbered and referred to in the text.

Mathematical formulas are expected to be as simple as possible and numbered in parentheses at the right margin. Non-Latin letters and hand-written symbols should be indicated and explained by making marginal notes in pencil.

Tables should be marked by Arabic numbers and printed in separate sheets together with their captions. Avoid too lengthy or complicated tables.

Figures should be drawn or printed in black and white, without legends, on separate sheets. The legends of figures should be printed as separate list. Good quality laser printings are preferred as master copies.

References: The text citation should contain the name(s) of the author(s) in Italic letter and the year of publication. In case of one author: *Miller* (1989), or if the name of the author cannot be fitted into the text: *(Miller,* 1989); in the case of two authors: *Gamov* and *Cleveland* (1973); if there are more than two authors: *Smith et al.* (1990). When referring to several papers published in the same year by the same author, the year of publication should be followed by letters a,b etc. At the end of the paper the list of references should be arranged alphabetically. For an article: the name(s) of author(s) in Italics, year, title of article, name of journal, volume number (the latter two in Italics) and pages. E.g. *Nathan, K.K.,* 1986: A note on the relationship between photosynthetically active radiation and cloud amount. *Időjárás 90*, 10-13. For a book: the name(s) of author(s), year, title of the book (all in Italics except the year), publisher and place of publication. E.g. *Junge, C. E.,* 1963: *Air Chemistry and Radioactivity*. Academic Press, New York and London.

The final version should be submitted on diskette altogether with one hard copy. Use standard 3.5" or 5.25" DOS formatted diskettes. The preferred word-processors are WordPerfect 5.1 and MS Word 6.0.

Reprints: authors receive 30 reprints free of charge. Additional reprints may be ordered at the authors' expense when sending back the proofs to the Editorial Office.

More information: gmajor@met.hu
Information on the last issues:
http://www.met.hu/firat/ido-e.html

Published by the Hungarian Meteorological Service

Budapest, Hungary

INDEX: 26 361

HU ISSN 0324-6329